# Naturally Occurring Proteins Direct Chiral Nanorod

# Aggregation

Lauren Warning,  $^{1,\dagger}$  Ali Rafiei Miandashti,  $^{1,\dagger}$  Anastasiia Misiura,  $^{1}$  Christy Landes,  $^{1,2,3,4,*}$  and Stephan Link  $^{1,2,3,*}$ 

<sup>1</sup>Department of Chemistry, Rice University, 6100 Main Street, Houston, TX 77005, USA

<sup>2</sup>Smalley Curl Institute, Rice University, 6100 Main Street, Houston, TX 77005, USA

<sup>3</sup>Department of Electrical and Computer Engineering, Rice University, 6100 Main Street,

Houston, TX 77005, USA

<sup>4</sup>Department of Chemical & Biomolecular Engineering, Rice University, 6100 Main Street,
Houston, TX 77005, USA

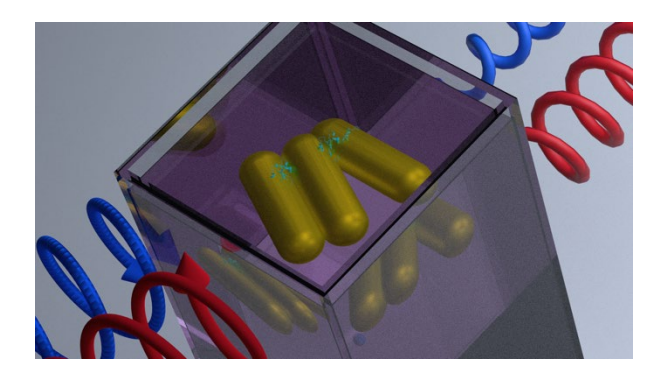
†Co-first Authors

\*Corresponding Authors: slink@rice.edu and cflandes@rice.edu

#### **Abstract**

Serum albumin can template gold nanorods into chiral assemblies, but the aggregation mechanism is not entirely understood. We used circular dichroism (CD) spectroscopy and scanning electron microscopy to investigate the role of protein identity/shape, protein/nanorod ratio, and surfactants on chiral protein-nanorod aggregation. Three globular proteins - serum albumin, immunoglobulin, transferrin - produced similarly sized chiral protein-nanorod aggregates. In solution these aggregates exhibited CD at the plasmon resonance that switched direction at specific protein/nanorod concentration ratios. Our explanation is that the extent of protein crowding influences protein conformation and therefore protein-protein interactions, which in turn direct nanorod aggregation into preferentially left- or right-handed structures. The fibrous proteins fibringen and fibrillar serum albumin also produced chiral nanorod aggregates, but did not exhibit a ratio-dependent switch in CD direction. Further, cetyltrimethylammonium bromide (CTAB) micelles prevented all aggregation, providing compelling evidence that protein-protein interactions are crucial for chiral protein-nanorod aggregate formation. The protein-dependent variations in CD and aggregation reported here present opportunities for future chiral nanostructure engineering and biosensing applications.

# **TOC Graphic**



**Keywords:** chiral assembly, nanoparticle assembly, plasmon-coupled circular dichroism, protein corona, chirality sensing

#### Introduction

Scientists have used various chemical and physical techniques to engineer plasmonic nanostructures over the past three decades. <sup>1-4</sup> Chiral plasmonic nanostructures have shown great potential for use in electronic devices, <sup>5</sup> biosensors, <sup>6-12</sup> and catalysis. <sup>13-17</sup> Due to the limited scalability of both top-down nanostructure fabrication techniques such as electron-beam lithography, <sup>18</sup> and bottom-up DNA-templated nanoparticle assembly, <sup>12, 19</sup> the assembly of achiral nanoparticles using naturally occurring chiral molecules is rapidly increasing. <sup>20-21</sup> Cellulose crystals, <sup>22-26</sup> organic nanofibers, <sup>27-30</sup> amino acids, <sup>31-32</sup> and peptides, <sup>33-36</sup> can be used to arrange plasmonic nanoparticles into chiral configurations. <sup>37</sup> For example, Tang and coworkers assembled gold nanorods (AuNRs) into 3D end-to-end nanochains with the aid of cysteine enantiomers because cysteine experiences preferential electrostatic attraction to AuNR tips. <sup>38</sup> Other peptide templates were used to self-assemble achiral gold nanoparticles into helical superstructures. <sup>34-36</sup>, <sup>39-43</sup>

Proteins are promising candidates for enabling nanoparticle assembly, but the mechanism of how they act as templates is not entirely understood. 44-46 Proteins readily adsorb to nanoparticles, modifying the nanoparticles' surface chemistry and physical properties. 46-50 Nanoparticles can also affect the protein's conformation and function, 47, 48 and can cause both protein and nanoparticle aggregation that may produce new chiral nanostructures. 46, 51-52 For example, bovine serum albumin (BSA) forms a protecting monolayer on AuNRs when the BSA/AuNR ratio is ~200K but instead AuNR aggregation occurs at BSA/AuNR ratios of ~50 because non-crowded BSA unfolds on the AuNR surfaces. 46 Additional reports suggest that serum albumin induces chiral AuNRs assemblies with abundant twisted side-by-side geometries. 44-45, 53

One complication in interpreting the mechanism driving protein-nanostructure aggregation is that CD at the plasmon resonance can arise from both structural chirality of the nanoparticles as well as from plasmon-coupled CD (PCCD), in which the chirality of the protein is transduced into a chiral signal at the plasmon resonance. 54-57 Cryo-transmission electron microscopy (TEM) characterization has provided evidence that serum albumin templates AuNR into structurally chiral assemblies. 45, 53 Zhang *et al.* identified contributions of PCCD in addition to structural chirality in BSA-AuNR aggregates, using a combined approach of single-particle CD spectroscopy, electron tomography, and electromagnetic simulations. 45 Interestingly, changes in chiroptical sign were observed for assemblies of CTAB-stabilized AuNRs interacting with serum albumin as parameters such as pH, protein surface charge, and solvent composition were varied. 44, 53 Wang *et al.* reported opposite ensemble CD signs from AuNR aggregates formed with serum albumin from different species, and their cryo-TEM reconstructions revealed twisted AuNR assemblies with opposite handedness. 53 The opposite signs were attributed to

differences in surface charge density among the different serum albumins. These findings suggest an important role of surface charge and chemical environment on the fate of protein-AuNRs assemblies and perhaps on the underlying mechanisms.

Some parameters that are especially worth exploring are protein identity, surface charge, protein/AuNR molar ratio, and AuNR ligands. 46, 58-60 There is limited information about chiral aggregates produced by serum proteins besides BSA and human serum albumin (HSA).<sup>44,53</sup> Protein shape, charge, and primary/secondary structure might drive AuNR aggregation through unique pathways or result in different chiral assemblies. Previous work suggests that protein density on AuNR surfaces is crucial to the aggregation process and influences the chiroptical signal exhibited by protein-AuNR assemblies. 44-45 Furthermore, nanoparticle functionalization can critically affect protein-nanoparticle interactions, often in the context of ligand charge. 61-62 Although both covalently and non-covalently bound AuNR ligands are studied in the literature, covalently-functionalized AuNRs are more promising for biological applications due to their decreased toxicity and higher cellular uptake than the commonly-used stabilizing surfactant CTAB.<sup>63</sup> Nevertheless, because AuNRs are frequently stabilized by ligands that are not covalently attached, 63-64 a protein's interaction with free ligands is important to consider. CTAB, a common surfactant that stabilizes AuNRs through van der Waals forces, 64 forms micelles that may influence protein stability and protein-AuNR interactions.<sup>45</sup>

Here, we report the use of extinction and CD spectroscopy combined with scanning electron microscopy (SEM) to address the following fundamental questions about chiral protein-nanoparticle assembly: (1) Are BSA and HSA unique in their ability to produce chiral protein-nanoparticle assemblies? (2) Is the handedness of the chiral protein-AuNR assemblies tunable? (3) Are there other parameters such as stabilizing agents that impact protein-AuNR assembly?

We examined the globular proteins HSA, immunoglobulin G (IgG), and transferrin (Tf) as well as the fibrous proteins fibrinogen (Fib) and fibrillar serum albumin. We evaluated the CD, aggregate size, and side-by-side ordering for all protein-AuNR assemblies to probe the effect of changing the protein/AuNR ratio, protein identity, and protein shape on the formation of chiral aggregates. Finally, we studied the effect of CTAB concentration on the CD from protein-AuNR assemblies to gain further insight into protein-AuNR interactions.

#### Methods

Materials. HSA (fraction V, 12668), IgG (from bovine serum, I5506), Tf (human, T3309), Fib (from human plasma, F3879), CTAB, cetyltrimethylammonium chloride (CTAC), 0.100 M phosphate buffer, and sodium citrate salt were acquired from Millipore-Sigma.

Mercaptoundecyltrimethylammonium bromide (MUTAB)-functionalized AuNRs (C12-40-650-TMU-DIH-50-1, manufacturer-reported dimensions: 40 x 80 nm) were purchased from Nanopartz. MUTAB-AuNRs, rather than CTAB-AuNRs, were necessary because some experiments required CTAB-free conditions, and the covalent modification protected AuNRs from aggregating in the buffer conditions. 5 M sodium chloride was obtained from Gibco. All samples were prepared in Biopur Eppendorf Lo-Bind centrifuge tubes.

Sample preparation. All protein solutions were reconstituted as 10 mg/mL stock solutions from lyophilized powder in 1 mM phosphate buffer at room temperature. Solutions were stored on ice while not in use. Less concentrated solutions were diluted from the stock solution. Protein concentrations ranged from 7.5  $\mu$ M (protein/AuNR = 140K) down to 27 pM (protein/AuNR = 0.51). The AuNR concentration was calculated based on the stock solution's concentration, reported by the manufacturer. CTAB and CTAC solutions were prepared with

Millipore water. For every CD experiment, two solutions—AuNR/surfactant (e.g., 3.5 μL AuNR from the stock solution + 96.5 μL 0.1 mM CTAB in water) and protein/buffer—were separately prepared a few minutes before each measurement. 100 μL of protein/buffer was added to 100 μL AuNR/surfactant, and the combined solution was mixed by lightly shaking, transferred to a 1 cm cuvette, and measured immediately. For most protein/AuNR ratios investigated, samples contained a final concentration of 0.5 mM phosphate buffer, 53 pM AuNR, and 0.05 mM CTAB or CTAC. This CTAB/CTAC concentration is lower than the critical micelle concentration (CMC) of ~0.92 mM.<sup>65</sup> To test the influence of surfactant concentration and phase, the amount of CTAB or CTAC was varied both below and above the CMC. Additional details can be found in the Supporting Information (SI).

HSA fibrils were produced using a protocol adapted from the literature. A 20 mg/mL HSA solution in 10 mM phosphate buffer was heated to 65 degrees Celsius for 48 hours. HSA fibrils were characterized via CD and fluorescence spectroscopy and fluorescence microscopy as described in the SI. The quantity of HSA fibrils is described in terms of the absolute concentration of HSA, which was estimated by comparing its absorbance at 280 nm to native HSA because the determination of the fibril concentration is challenging due to fibril size heterogeneity.

**Extinction and CD spectroscopy.** Baseline-corrected CD and extinction spectra were collected on a J-815 JASCO CD spectrometer. The AuNR-containing spectra shown in both the main text and SI were collected using the following parameters: 1 cm path length quartz cuvette, 200 nm/min scan rate, 10.0 nm bandwidth, 1.0 nm data pitch (one data point was collected per 1.0 nm), 1 sec digital integration time (DIT), 3 scans to average over a wavelength range of 200-850 nm. Each measurement took 10 min to complete. Extinction and CD magnitude decreased

over time,<sup>45</sup> but otherwise did not change significantly over the three acquisitions. When collecting protein-only spectra in the ultraviolet spectral range, the parameters were changed to: 1 cm path length quartz cuvette, 50 nm/min scan rate, 2.0 bandwidth, 1.0 data pitch, 1 sec DIT, 3 scans to average over a wavelength range of 200-250 nm. Additional data collection details are available in the SI.

Spectra were processed using a home-written code in MATLAB. The instrument calculates CD ( $\Delta A$ ) and extinction (A) based on the following equations:

$$\Delta A = A_{L-CPL} - A_{R-CPL} \tag{1}$$

$$A = (A_{L-CPL} + A_{R-CPL}) / 2 \tag{2}$$

 $A_{L/R-CPL}$  is the extinction of left- or right-handed circularly polarized light (CPL). It is worth noting that AuNRs are strong scatterers and thus the CD we report is the combination of absorption and scattering of incident CPL. The instrument reports CD in millidegrees (mdeg), and extinction is unit-less. We normalized all protein-AuNR extinction spectra to the AuNR-only extinction at 400 nm, which corresponds to Au's inter-band transitions as an indicator of Au concentration. We also presented the CD spectra using Kuhn's dissymmetry, or g-factor. First, we converted CD to the appropriate absorbance "units" (32980 mdeg = 1 absorbance "unit"), and then calculated the g-factor with the following equation:

$$g = \Delta A / A \tag{3}$$

Note that we used the raw, not normalized, extinction values for this calculation. In addition to extinction, CD, and g-factor spectra, the maximum g-factor values observed for the shortest wavelength major CD peak, between 600-700 nm, were extracted from the spectra of protein-AuNR assemblies to be presented as a function of protein or surfactant concentration.

**SEM.** Samples were prepared on indexed indium tin oxide substrates. We marked the substrates by evaporating a 20-nm Ti layer on glass slides with an attached index grid (Structure Probe, Inc.) and subsequently removing the grid. The slides were sonicated in Liquinox and ethanol for 7 min each, followed by drying with nitrogen gas. Slides were plasma cleaned for 3 min under oxygen (PDC-32G; Harrick Plasma; medium power). Protein-AuNR solutions were mixed and incubated for 30 sec before 50 μL was drop-casted onto a cleaned slide and spin-coated for 1 min. The remaining 150 μL solution was transferred to a cuvette to collect the CD spectrum (~90 sec after the initial mixing). The SEM images were collected on an FEI Helios NanoLab 660 DualBeam system.

Protein-AuNR aggregates were analyzed based on number of AuNRs per aggregate and side-by-side ordering using a previously defined method. 45, 69 Comparisons were performed using the two-sample Kolmogorov-Smirnov (K-S) test for non-normal data reported in the Supporting Information.

#### **Results and Discussion**

# Globular Serum Proteins Produce Similar Chiral Protein-AuNR Aggregates

HSA induced AuNR aggregation to produce CD-active complexes with the HSA/AuNR ratio affecting CD magnitude and direction. Figure 1 illustrates the extinction, CD, and g-factor spectra of HSA-AuNR aggregates at varied HSA/AuNR ratios. The g-factor reports CD normalized by extinction, as defined in the Methods section. Note that our reported CD represents the differential extinction, rather than true absorption of circularly polarized light due to the fact that AuNRs are strong scatterers. The AuNR concentration was held constant at 53 pM, while the HSA concentration was varied between 0 and 3.75 µM to tune the HSA/AuNR

ratio, while remaining far below the physiological concentration of  $\sim$ 650  $\mu$ M associated with stable colloids. The extinction and CD spectra of pure AuNRs matched expectations for monodisperse AuNRs. The extinction and CD spectra of pure AuNRs matched expectations for monodisperse AuNRs. The extinction and the absence of CD (Figure 1B-C). In Figure S1, we show the size analysis of AuNRs having averages dimension of 36 x 79 nm. Redshifted extinction seen at HSA/AuNR = 71K indicates the adsorption of HSA on the AuNR surface. At HSA/AuNR ratios of 14K to 710, AuNR extinction decreased and further redshifted, which is consistent with aggregation. Additionally, CD developed with a negative peak at  $\sim$ 610 nm and a positive peak at  $\sim$ 780 nm. This bisignate lineshape is described as a positive Cotton effect. The extinction and CD spectra together suggest the formation of HSA-AuNR aggregates. The largest negative CD occurred when HSA/AuNR = 1.4 K. For this range of HSA/AuNR ratios, the spectral shape of the CD and the trend with changing protein concentration are consistent with previously published work.

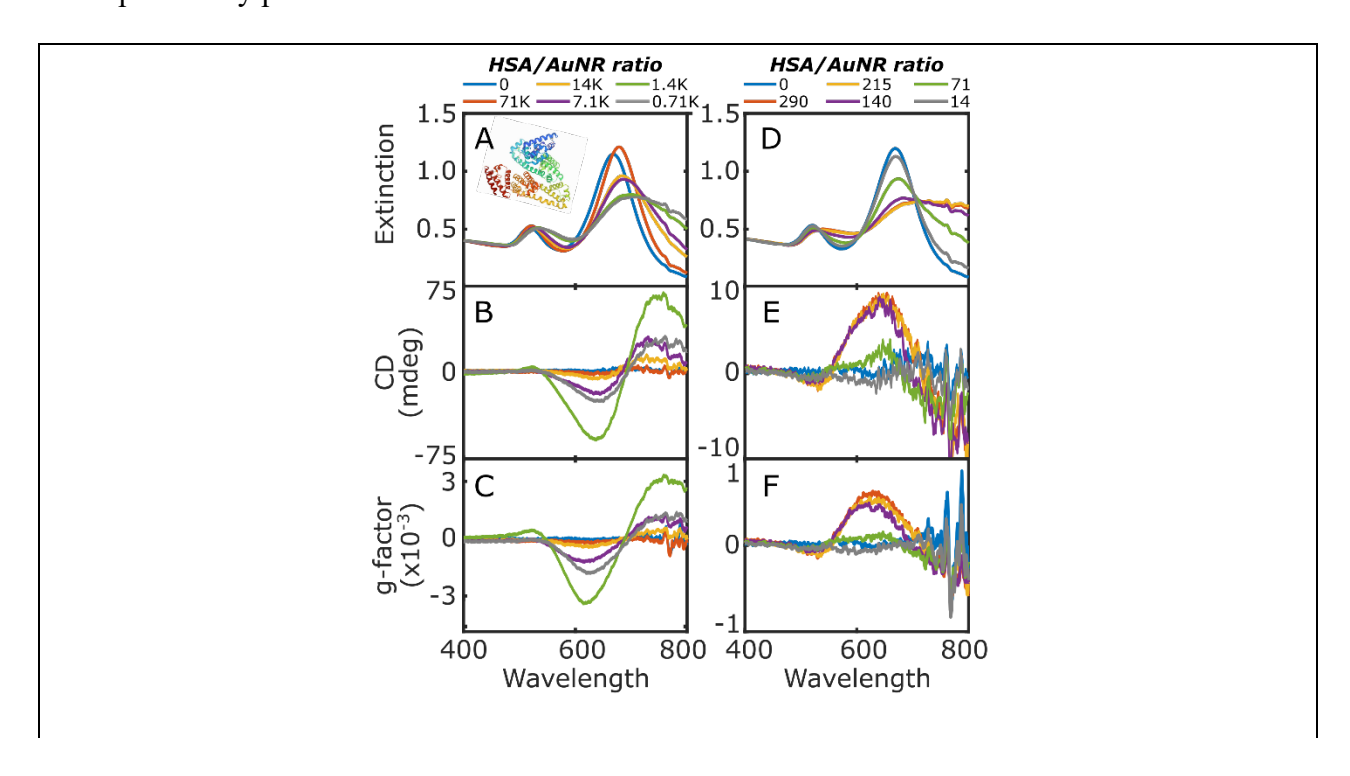


Figure 1: HSA induces AuNR aggregation and the chiroptical signal is modulated with the HSA/AuNR ratio. (A) Extinction, (B) CD, and (C) g-factor spectra of HSA-AuNR aggregates at HSA/AuNR ratios ranging from 71K to 710. (D) Extinction, (E) CD, and (F) g-factor spectra of HSA-AuNR aggregates at lower HSA/AuNR ratios ranging from 290 to 14. Note the different y-axis scales in panels B&E and C&F. All samples were measured ~30 sec after HSA and AuNRs were combined and contained 0.5 mM phosphate and 0.05 mM CTAB. Extinction spectra were normalized at 400 nm to the AuNR-only sample. The noise observed at wavelengths longer than 700 nm was due to the decreased sensitivity of the detector and the low intensity of the Xe lamp. HSA's crystal structure in panel A was obtained from the Protein Data Bank (1BM0).<sup>74</sup>

Interestingly, we observed that the HSA-AuNR complexes had the opposite CD sign when the HSA/AuNR ratio was lowered below 710. Figure 1D-F shows the extinction, CD, and g-factor spectra for HSA/AuNR ratios ranging from 290 to 14. When the HSA/AuNR ratio was lowered from 710 (Figure 1B) to 290 (Figure 1E), the chiroptical signal at ~650 nm flipped from negative to positive. In this HSA/AuNR ratio regime of 290 to 14, the complexes produced a bisignate lineshape with maximum CD at ~620 and minimum CD at ~800 nm, illustrating a negative Cotton effect. The SA/AuNR ratios  $\geq$  710, the samples with the largest CD generally exhibited the lowest extinction and the most redshifted extinction maximum compared to the HSA/AuNR = 0 control, indicating aggregation. The largest positive CD magnitude occurred at HSA/AuNR = 290. The aggregates with a positive Cotton effect (Figure 1C) had larger g-factors than those displaying a negative Cotton effect (Figure 1F). In the

following discussion, we refer to the protein/AuNR ratio at which a CD sign reversal occurred as the "critical concentration ratio."

The observed CD behavior for the entire range of HSA/AuNR ratios studied was reproducible. In Figure S2, we summarize the results for four HSA/AuNR concentration ratio experiments performed, twice with CTAB and twice with CTAC. The use of CTAB versus CTAC will be further discussed below. Our reproducible observations of a sign flip at a critical concentration ratio are consistent with an earlier report. Shinmori *et al.* reported a sign flip when they monitored the CD of CTAB-stabilized AuNRs with varying concentrations of HSA in a solution containing 20% acetonitrile.<sup>44</sup> They also observed a change in CD sign when the fraction of acetonitrile was varied and suggested the preferential production of oppositely-handed chiral structures because of a decrease in electrostatic repulsion of CTAB molecules from the AuNR surface in acetonitrile.

Like HSA, IgG and Tf also produced chiral AuNR aggregates that experienced a change in CD sign at a critical concentration ratio. We tested protein/AuNR ratios ranging from 0 to 7.5  $\mu$ M (below physiological conditions for IgG of ~70  $\mu$ M and Tf of ~35  $\mu$ M<sup>70</sup>). The extinction and g-factor spectra of IgG and Tf are given in Figure 2. Again, the two columns show protein-AuNR complexes above and below the critical protein/AuNR ratio at which the CD sign inverted. The majority of IgG- and Tf-AuNR extinction spectra exhibited redshifts and decreased magnitudes compared to AuNRs without proteins, indicating AuNR aggregation. Although extinction differed between IgG and Tf, the observed CD trends were similar. IgG's maximum negative and positive g-factors observed at the shorter wavelength peak occurred when IgG/AuNR = 29K (Figure 2B) and 1.4K (Figure 2D), respectively. Tf's maximum negative and positive g-factors arose when Tf/AuNR = 7.1K (Figure 2F) and 290 (Figure 2H), respectively.

The IgG-AuNR aggregates in Figure 2D showed evidence of an additional sign flip back to a positive Cotton effect at IgG/AuNR ≤ 140, but the magnitude of this signal was minimal compared to the other regimes of IgG/AuNR ratio. It is worth noting that at protein/AuNRs ratios ≥ 71K, HSA forms a stabilizing layer around the AuNRs and results in the observation of no CD signal (Figure 1A-B), while IgG and Tf continue to destabilize the AuNRs and produce chiral aggregates at the highest protein concentrations tested (Figure 2A-B&E-F).

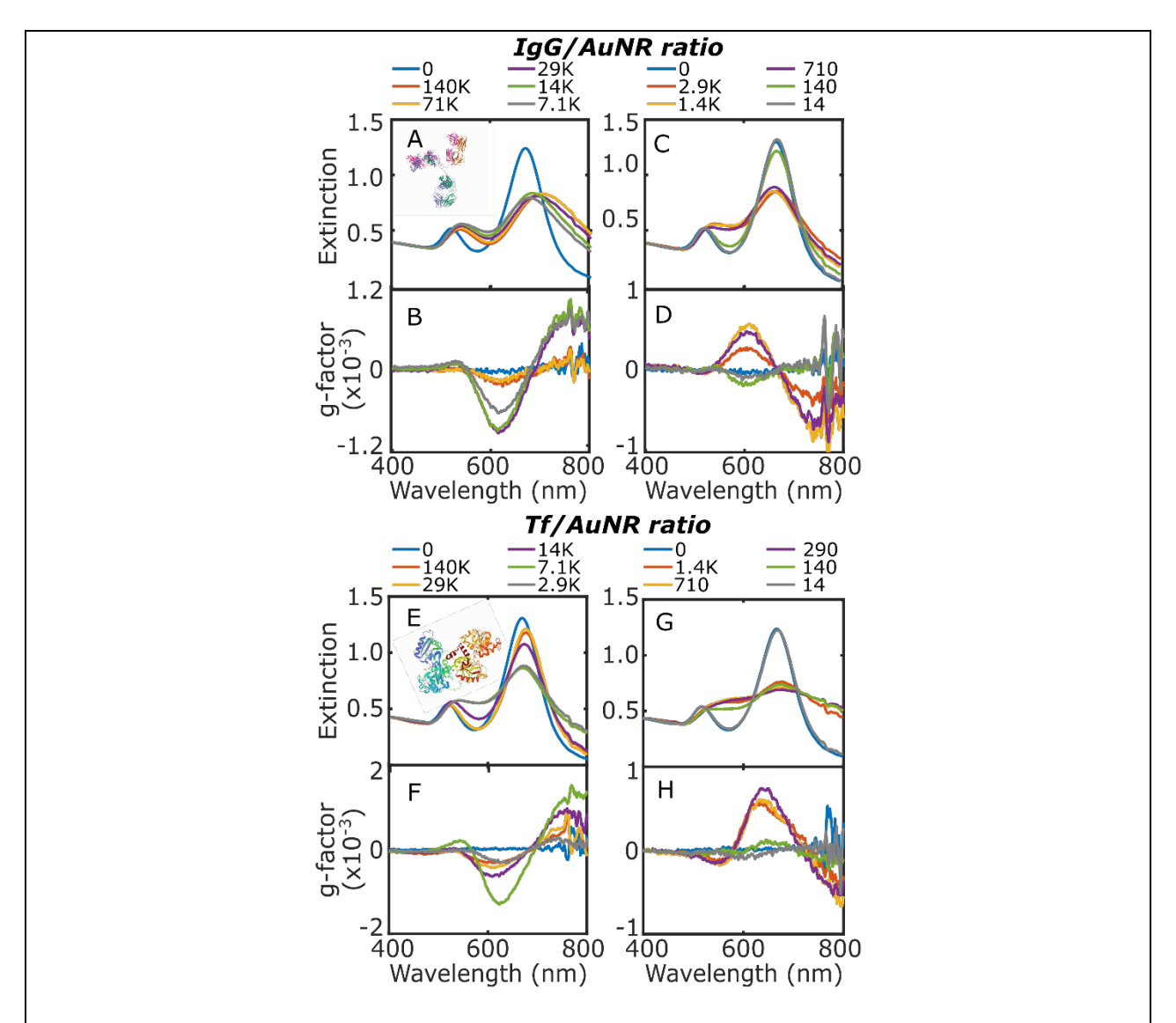
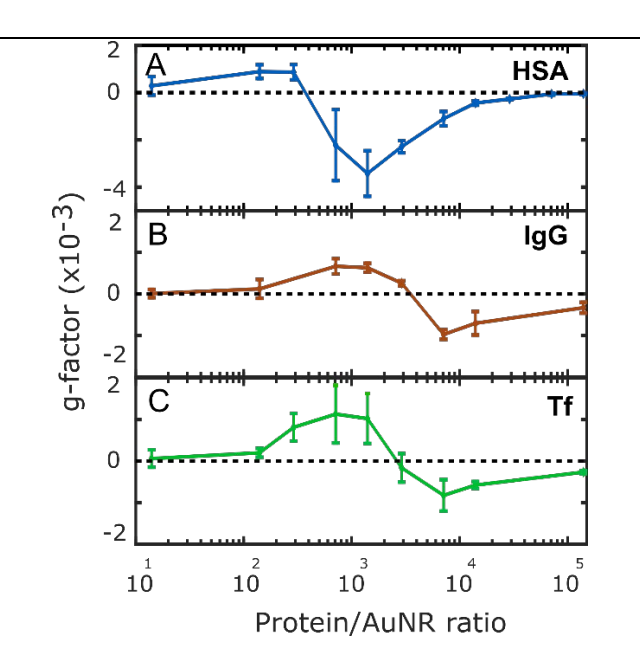


Figure 2: IgG and Tf induce AuNR aggregation and the chiroptical signal is modulated with protein/AuNR ratio. (A) Extinction and (B) g-factor spectra of IgG-AuNR aggregates

at IgG/AuNR ratios of 140K to 7.1K. (C) Extinction and (D) g-factor spectra of IgG-AuNR aggregates at lower IgG/AuNR ratios of 2.9K to 14. (E) Extinction and (F) g-factor spectra of Tf-AuNR aggregates at Tf/AuNR ratios of 140K to 2.9K. (G) Extinction, and (H) g-factor spectra of Tf-AuNR aggregates at lower Tf/AuNR ratios of 1.4K to 14. Note the different y-axis scales in panels B&D and F&H. All samples were measured ~30 sec after proteins and AuNRs were combined and contained 0.5 mM phosphate and 0.05 mM CTAB. Extinction spectra were normalized at 400 nm to the AuNR-only sample. The IgG and Tf crystal structures in (A) and (E) were obtained from the Protein Data Bank (1IGT & 2HAV). 75-76

HSA, IgG, and Tf experienced similar CD behavior as the protein/AuNR ratio was varied. In Figure 3, we summarize the maximum g-factors generated by protein-AuNR aggregates as a function of the protein/AuNR ratio. The reported values are the average of the maximum absolute g-factors (positive or negative), and the error bars quantify the standard deviation from triplicate trials. Sample-to-sample magnitude variation is attributed to the non-equilibrium nature of the aggregation. HSA, IgG, and Tf all produced protein-AuNR complexes with negative Cotton effects below the critical protein/AuNR ratio and positive Cotton effects above. HSA exhibited the CD sign crossover at HSA/AuNR =  $\sim$ 400, while for IgG and Tf the sign flipped between protein/AuNR =  $\sim$ 2K and  $\sim$ 4K, an order of magnitude higher than for HSA. The absolute magnitude of the g-factor varied from protein to protein but was of the same order. Among multiple trials with either CTAB or CTAC (Figure S2), HSA consistently produced the largest negative signal compared to IgG and Tf (g = .004 versus -.001 and -.002).



**Figure 3: Maximum g-factor for varying protein/AuNR ratios.** The largest g-factor magnitude and sign for the major short-wavelength maximum or minimum between 600 and 700 nm as a function of protein/AuNR ratio for (A) HSA, (B) IgG, and (C) Tf. Values and error bars represent the mean and standard deviation of triplicate data.

The entire protein/AuNR ratio study was performed at least three times, twice with CTAB and at least once with CTAC, to show that the observed behaviors were reproducible (Figure S2). The trend of positive CD at lower protein/AuNR ratios and negative CD at higher ratios remained consistent. The close match observed for CTAB and CTAC suggests that if the surfactants' presence affected the aggregation, they did so in the same fashion.

SEM analysis suggests that globular protein-AuNR aggregates were similar even when protein/AuNR ratio and protein identity were varied. Previous work applied SEM to characterize AuNR aggregate geometries and identified different structural patterns for AuNRs aggregated with salt versus protein. 45, 69 Here, we similarly characterized protein-AuNR aggregates at the protein/AuNR ratios that produced the largest positive and negative g-factors using SEM (Figure

4) to determine whether the changes in optical chirality correlate with structural patterns. AuNR aggregates existed in varying geometries, including side-by-side AuNR arrangements. We assessed distributions of the number of AuNRs per protein-AuNR aggregate (Figure 4C, F, &I; Tables S1&S2) as well as side-by-side ordering per aggregate (Figure S3) and observed no apparent correlation between aggregate size and ordering with the CD sign observed from protein-AuNR aggregates. Further details and discussion are available in the SI.

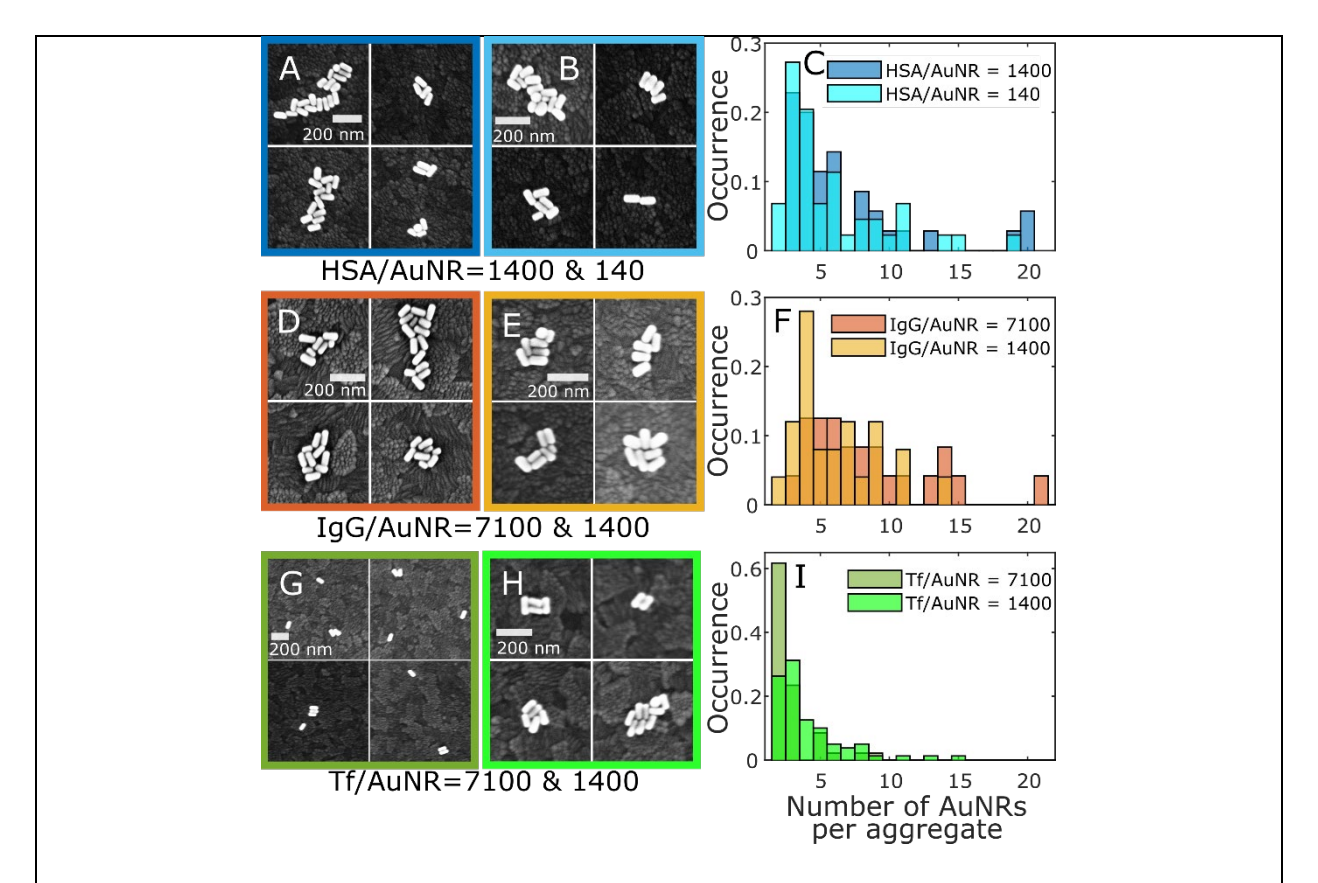


Figure 4: Globular protein-induced AuNR aggregates produced closely packed assemblies. Representative SEM micrographs of HSA-AuNR aggregates for HSA/AuNR = 1.4K (A) and 140 (B). (C) Distributions of the number of AuNRs per aggregate. SEM micrographs and aggregate size distributions for IgG-AuNR (D-F) and Tf-AuNR (G-I) aggregates at protein/AuNR ratios = 7100 and 1400. Note that the y-limits in panel I are

different than in C and F. These protein/AuNR ratios were selected because they produced the largest g-factors. The associated extinction and g-factor spectra, which were collected  $\sim$ 1 min after the samples were spin-cast onto the substrate, are available in Figure S4A-C. Each sample's mean, standard deviation, and N is reported in Table S2.

Our results not only demonstrate that IgG and Tf, in addition to HSA, produce chiral AuNR assemblies, but also suggest that the three globular proteins follow a similar aggregation mechanism. HSA, IgG, and Tf all exhibited a CD sign reversal at unique, critical protein/AuNR ratios, and the aggregates they formed had indistinguishable aggregate sizes (Figure 4, Table S1). We postulate that these similarities occurred because HSA, IgG, and Tf share several characteristics: they are globular and have a net negative charge. The Acontains primarily  $\alpha$ helical secondary structure, <sup>78</sup> Tf contains  $\alpha$ -helical and  $\beta$ -sheet structures, <sup>79</sup> and IgG contains primarily β-sheets. <sup>56</sup> Figure S5 shows that HSA, IgG, and Tf all have negative CD in the far UV spectral region, as is expected for both  $\alpha$ -helical and  $\beta$ -sheet structures. The shapes of HSA and Tf are also fairly similar: HSA (Figure 1A inset) is described as a triangular prism (roughly 8 x 8 x 3 nm)<sup>78</sup> with a hydrodynamic radius of 3.5 nm.<sup>80</sup> Tf (Figure 2E inset) has two lobes (2.1 x 2.5 x 3.5 nm per lobe)<sup>79</sup> and overall a 3.7 nm hydrodynamic radius.<sup>80</sup> IgG's Y-shape (Figure 2A inset) is distinct (14.5 x 8.5 x 4.0 nm), 81 though globular, with a hydrodynamic radius of 5.5 nm. 82 Shinmori et al. previously reported that globulin produced chiral AuNR aggregates, 44 but to our knowledge, our study presents the first in-depth comparison of different serum proteins templating AuNR assembly as a function of protein/AuNR ratio.

Fibrous Fibrinogen Aggregates Template AuNR Assembly Without a Sign Flip

Like the globular proteins, Fib also induced chiral AuNR assembly. However, Fib experienced a different variation in CD sign as the protein/AuNR ratio was tuned compared to the globular proteins. Unlike the globular proteins, Fib is fibrous with a long, rod-like shape (~47 nm length, ~9 nm diameter) and it is twice as large as the largest globular protein, IgG (340 kDa versus 150 kDa). 81,83 Fib's extended length exceeds and approaches the 36 nm width and 79 nm length of the AuNRs. Figure 5A-B shows that Fib-AuNR complexes produced no CD when Fib/AuNR > 21K and negative Cotton effects when Fib/AuNR < 5.1K. This result contrasts with the globular proteins, which produced positive Cotton effects for protein/AuNR > ~1K. Fib-AuNR complexes also exhibited negative Cotton effects at even lower Fib/AuNR ratios (< 340, Figure 5C-D). The maximum g-factor,  $\sim 0.005$ , occurred at Fib/AuNR = 510 and surpassed the magnitude of the globular protein-AuNR complexes with negative Cotton effects. Although there was some variability in CD at Fib/AuNR ratios < 510 (Figure S2), Fib-AuNR complexes reproducibly gave negligible CD or negative Cotton effects at Fib/AuNR ratios > 510. Moreover, at Fib/AuNR ratios > 21K ( $> 1 \mu$ M, approaching Fib's physiological concentration of  $\sim 6 \mu$ M),  $^{70}$ extinction spectra suggest that AuNRs aggregate, but no net CD was observed (Figure 5A-B). We found that when Fib/AuNR = 5, Fib did not create chiral NRs assemblies (Figure 5C-D). This observation is consistent with globular protein-AuNR aggregates in the lowest concentration ratio range.

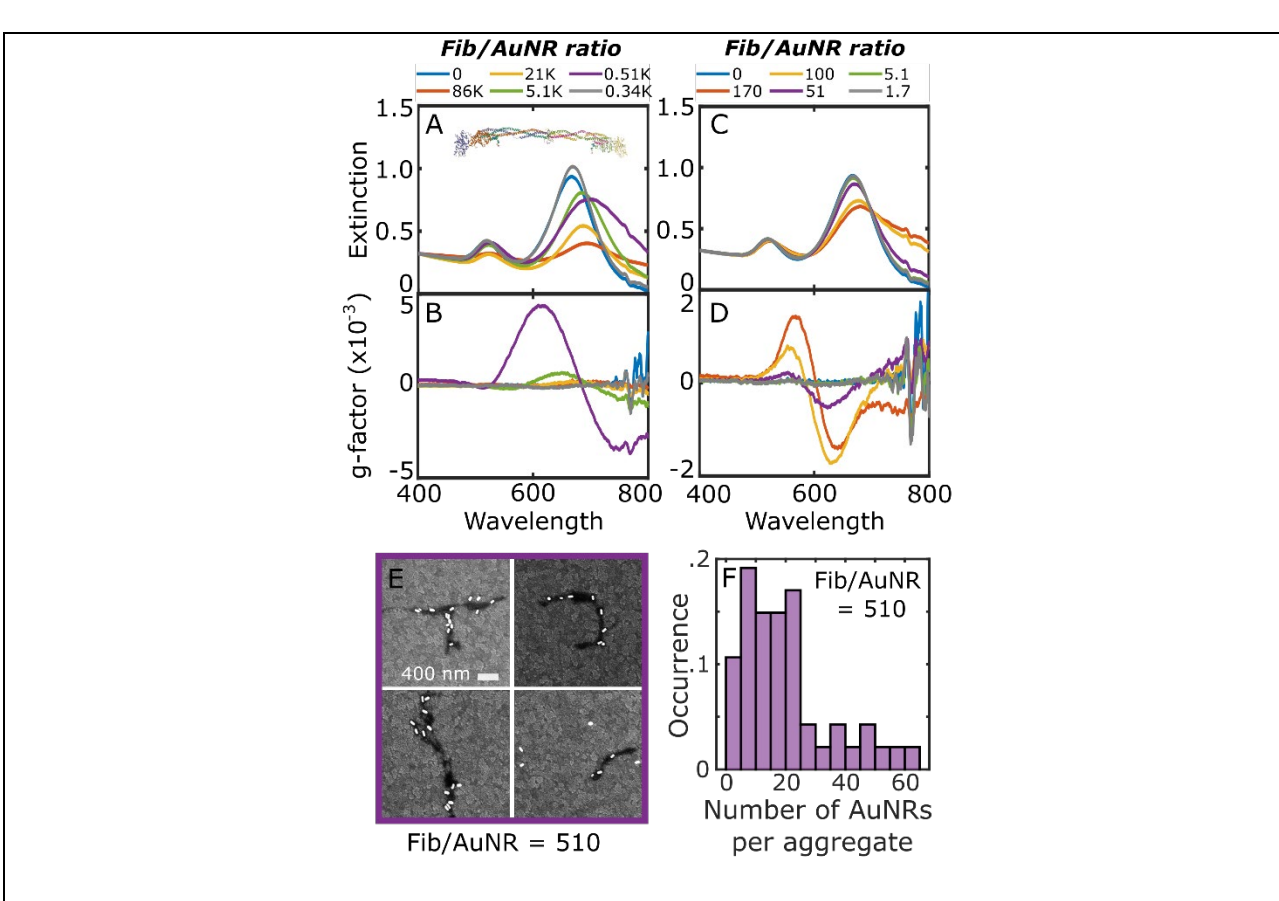


Figure 5: Fib-induced AuNR aggregates produced a large chiroptical signal and large fibrous configurations. (A) Extinction and (B) g-factor spectra of Fib-AuNR aggregates as a function of Fib/AuNR ratios, varying from 86K to 0.34K. (C) Extinction and (D) g-factor spectra of Fib-AuNR aggregates as a function of lower Fib/AuNR ratios, varying from 170 to 1.7. All samples were measured ~30 sec after Fib and AuNRs were combined and contained 0.5 mM phosphate and 0.05 mM CTAB. Extinction spectra were normalized at 400 nm to the AuNR-only sample. (E) Representative SEM images of Fib-AuNR aggregates prepared with Fib/AuNR = 510. The CD of this sample was measured ~90 sec after mixing and can be found in Figure S4D. (F) The number of AuNRs per Fib-AuNR aggregate (N = 47, mean = 20.0, standard deviation = 15). Fib's crystal structure shown in panel A was obtained from the Protein Data Bank (3GHG).<sup>84</sup>

Fib further distinguishes itself from the globular proteins based on its ability to produce CD when salt was present. The lyophilized Fib used contained ~25% sodium chloride and ~15% sodium citrate, while the globular proteins were salt-free. We mimicked these salt conditions and performed a side-by-side study of HSA-AuNR aggregation with and without salt and found that the salt prevented the formation of CD (Figure S6). This result suggests that the presence of salt does not explain Fib's distinct aggregation behavior. Further, it implies that Fib more efficiently produced CD-active protein-AuNR aggregates than HSA.

SEM characterization of Fib-AuNR aggregates prepared at Fib/AuNR = 510, when the g-factor was maximized, revealed a distinct morphology compared to the globular proteins. Unlike the globular protein-AuNR aggregates shown in Figure 4, AuNRs adsorbed to dark fibrous superstructures (Figure 5E). These fibrous superstructures were also present in the absence of AuNRs, indicating that the AuNRs are not responsible for these architectures (Figure S7). Based on their large size, which exceeded the 47 nm length and 9 nm width of a single Fib molecule, <sup>84</sup> these superstructures must be aggregates of several Fib proteins. Fib-AuNR aggregates exhibited a larger range of aggregate sizes (mean value = 20.0 AuNRs per aggregate, Figure 5F) than globular protein-AuNR aggregates (mean values varied between 2.9 and 9.0 AuNRs per aggregate, Figure 4), likely due to the large size of the fibrous Fib superstructures. Further, the Fib-AuNR complexes qualitatively appeared more spread apart, which could explain their decreased side-by-side ordering (Figures S3, S8) compared to the globular proteins that created more compact, smaller aggregates.

Interestingly, previous studies of AuNR dimers with defined geometries indicate that the longitudinal surface plasmon resonance coincides with the zero crossing of the bisignate CD in both PCCD-active and structurally chiral dimers. <sup>13, 85-86</sup> In the current work, there are small shifts

between the plasmon resonance and zero crossing of the bisignate CD, likely indicating heterogeneity among aggregate geometry and/or protein conformation. Specifically, we observed the zero crossing of the bisignate CD is blue shifted for the Fib-AuNR samples, particularly for the low Fib/AuNR ratio. Increased heterogeneity is also consistent with the SEM images showing less defined aggregates.

# Fibrillar HSA Provides Insight on Globular versus Fibrous Protein-AuNR Aggregation

To better understand the structural role of globular and fibrous protein architectures in protein-AuNR aggregates, we induced fibrillation in one of the globular proteins (HSA) and compared its behavior after mixing with AuNRs to globular protein-AuNR and Fib-AuNR aggregates. Numerous studies have established HSA as a model protein for fibrillation, <sup>66-67</sup> and we confirmed the successful formation of HSA fibrils using a variety of techniques (Figure S9).

We performed native and fibrillar HSA-AuNR experiments side-by-side and found that their chiroptical behavior differed. As with the other protein samples, we varied HSA fibril concentration via dilutions in the buffer. The concentration of HSA in the HSA fibril solutions was estimated based on the sample's absorbance at 280 nm and was compared to native HSA at matched concentrations. The true concentration of fibrils is challenging to estimate due to fibril size heterogeneity. Fibrillar HSA-AuNR aggregates showed attenuated g-factors compared to native HSA, and the positive Cotton effect g-factors at HSA/AuNR ratios >2000 were absent (Figure 6A). Figure 6A summarizes the maximum g-factor of native and fibrillar HSA-AuNR mixtures as a function of the HSA/AuNR ratio within the spectral range of 600-700 nm. Native HSA reproduced the behavior described in Figure 3A, *i.e.* negative g-factors (from positive Cotton effects) at HSA/AuNR = 720-2800 and positive g-factors (from negative Cotton effects)

at HSA/AuNR = 72-280. A small negative g-factor tended to appear at even lower HSA/AuNR ratios (Figure 6A, HSA/AuNR <100), a behavior that was also noted in the IgG-AuNR aggregates (Figure 2D). In contrast, the HSA fibril samples exhibited negligible g-factors at HSA/AuNR = 1400-2800, positive g-factors from negative Cotton effects at HSA/AuNR = 280-720, and negative g-factors from positive Cotton effects at HSA/AuNR = 28-140. The exact HSA/AuNR ratio at which the maximum g-factor within each concentration regime occurred varied from sample to sample. We therefore report the largest g-factor produced per sample in each protein/AuNR ratio regime in Figure 6B as a bar chart, in which the values and error bars represent the mean and standard deviation of triplicate data. Native HSA-AuNR aggregates always showed significantly larger g-factors than fibrillar HSA-AuNR aggregates in the highest two protein/AuNR ratio regimes. For HSA/AuNR = ~2000, native HSA-AuNR aggregates gave g-factors on the order of 0.003 while fibrillar HSA-AuNR aggregates displayed negligible g-factors. When HSA/AuNR = ~500, the native HSA-AuNR aggregates produced a mean g-factor that was ~6 times larger than that of the fibrillar HSA-AuNR aggregates.

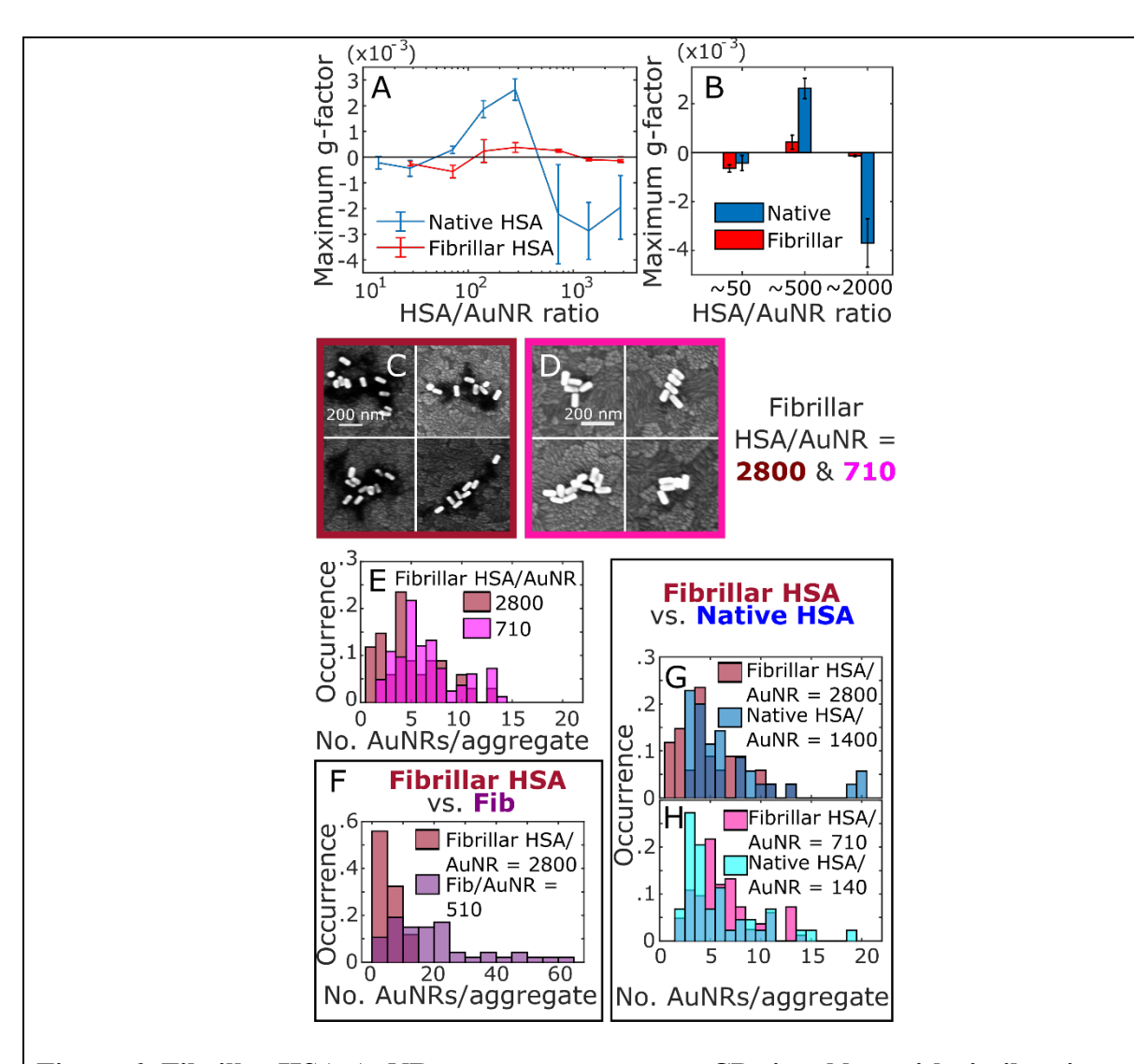


Figure 6: Fibrillar HSA-AuNR aggregates attenuate CD signal but with similar sign as

**Fib-AuNRs.** (A) Maximum g-factors at the major short-wavelength peak/trough between 600-700 nm in native and fibrillar HSA-AuNR aggregates as a function of HSA/AuNR ratio. Data points and error bars represent the mean and standard deviation of triplicate measurements. (B) Maximum g-factors achieved per data set as the exact concentration of the maximum signal varied slightly from experiment to experiment. Bar chart values and error bars represent mean and standard deviation from triplicate experiments. (C-D) Representative SEM micrographs for fibrillar HSA-AuNR aggregates when HSA/AuNR = 2800 (C) and 710 (D). The 2800 ratio

produced a positive Cotton effect with the native HSA, but gave no CD here. The 710 ratio yielded an attenuated negative Cotton effect. Corresponding CD spectra are given in Figure S4E. (E-H) Histograms comparing the number of AuNRs per protein-AuNR aggregate, as determined via SEM: (E) Comparing fibrillar HSA at the HSA/AuNR ratios imaged in panels C and D (2800: N = 34, mean = 4.9; 710: N = 83, mean = 6.5; K-S test: p = 0.02, distinguishable); (F) Comparing fibrillar HSA (2800) to Fib (510), shown in Fig. 5F (N = 47, mean = 20.0; K-S test: p = 0.00, distinguishable); (G,H) Comparing fibrillar and native HSA-AuNR aggregates at relatively high (native HSA 1400: N = 35, mean = 6.8; p = 0.15, indistinguishable) and low concentrations (native HSA 140: N = 44, mean = 5.8; p = 0.01, distinguishable). Buffer conditions for all samples shown were 0.5 mM phosphate and 0.05 mM CTAB. A summary of statistical values is provided in Tables S1&2.

The fibrillar HSA-AuNR aggregates are comparable to the Fib-AuNR aggregates based on chiroptical behavior and morphological features. HSA fibrils and Fib did not produce negative g-factors from positive Cotton effects for protein/AuNR > 5100, but they showed CD at lower protein/AuNR ratios (Figures 5A-B & 6A). Figure 6C-D shows representative SEM micrographs of fibrillar HSA-AuNR aggregates when HSA/AuNR = 2800 and 710, with associated spectra given in Figure S4E. The low contrast dark shapes visible for fibrillar HSA/AuNR = 2800 were like those observed in Fib-AuNR aggregates (Figure 5E), although the fibrillar HSA structures were more compact while the Fib superstructures were long and thin. Further, Fib-AuNR aggregates were significantly larger than fibrillar HSA-AuNR aggregates (Figure 6F, means = 20.0 and 4.9, respectively; K-S test: p = 0.00).

The fibrillar HSA-AuNR aggregates at HSA/AuNR = 2800 and 710 exhibited different chiroptical behavior and aggregate morphology. The fibrillar HSA/AuNR = 710 aggregates produced CD and were morphologically like the globular protein-AuNR aggregates in Figure 4 that featured tightly packed AuNR clusters. The fibrillar HSA-AuNR aggregates at the 2800 ratio possessed fewer AuNRs per protein-AuNR aggregate than at the 710 ratio (Figure 6E, means = 4.9 and 6.5; K-S test: p = 0.02). Comparisons of the native and fibrillar HSA-AuNR aggregate sizes are described in Figure 6G-H, which revealed that at the lower HSA/AuNR ratio tested, fibrillar HSA-AuNR aggregates were bigger than native HSA-AuNR aggregates, while at the higher concentration the number of AuNRs per protein-AuNR aggregate was similar.

# Chirality Origins in Protein-AuNR Aggregates

The change in CD sign and magnitude observed as the globular protein/AuNR ratio was tuned (Figure 3) suggests that protein-AuNR aggregate CD depends on protein density. A protein's conformation can be influenced by the crowded nature of its environment in solution and at surfaces. <sup>87-89</sup> Varied orientations and conformations of surface-adsorbed proteins can expose different structural motifs that change the protein's interaction with its environment. <sup>90-91</sup> Protein density also influences nanomaterial stability. <sup>92-93</sup> HSA and Tf are present at concentrations of ~600  $\mu$ M and ~30  $\mu$ M in the human body. <sup>70</sup> At concentrations closer to physiological conditions than those studied in this report (7.5  $\mu$ M), HSA and Tf can form a monolayer on the nanoparticles that protects against aggregation. <sup>93-96</sup> Note that we quote absolute protein concentrations because protein/nanoparticle ratios may not be directly comparable for particles of different shapes and sizes. The phenomenon of protein-induced nanoparticle aggregation at lower protein/AuNR ratios has been attributed to increased protein

unfolding due to decreased crowding on the surface of the nanoparticles.<sup>46, 93</sup> Therefore, we suggest that the switch in CD sign observed at a critical protein/AuNR ratio is related to changes in protein conformation occurring because of the presence or absence of protein crowding.

Biomolecule-nanoparticle systems produce CD by two major mechanisms: interactions between the plasmons of nanoparticles oriented in chiral geometries (structural chirality)<sup>97-101</sup> and chiral molecular charge motion inducing chirality in the plasmon oscillation, yielding a chiroptical signal (PCCD).<sup>54, 56, 101</sup> Although chiral molecules can template nanoparticle assemblies with preferential handedness, CD attributed to structural chirality relies only on nanoparticle properties such as size, inter-particle separation, and twist angle.<sup>97</sup> In contrast, PCCD's magnitude also relies on the chiral molecule's properties such as quantity,<sup>102</sup> orientation,<sup>54-55</sup> and, in many cases, presence within a hotspot between two nanoparticles.<sup>37, 57, 85</sup> Systems that have produced strong PCCD were carefully engineered to meet these criteria, such as discrete nanoparticles functionalized with self-assembled monolayers of chiral molecules and AuNR assemblies with uniformly oriented chiral molecules within the gaps.<sup>38, 85, 103</sup>

Structural chirality is a likely contributor to the ensemble CD from protein-AuNR aggregates reported here because of the anisotropic nature of AuNRs and literature evidence of structurally chiral protein-AuNR assemblies,<sup>53</sup> but PCCD could equally play a role.<sup>45</sup> Cholate-Ag nanosphere aggregates have previously been shown to exhibit strong CD attributed to the PCCD mechanism,<sup>57</sup> while the CD from nanochains consisting of anisotropic AuNRs linked by thiolated biomolecules has been attributed to both PCCD<sup>38, 103-104</sup> and structural chirality.<sup>105</sup> In addition, DNA origami, a tool used to engineer chiral assemblies, was used to synthesize AuNR dimers that produced CD via both structural chirality and PCCD, and the CD magnitudes of both mechanisms were comparable.<sup>101</sup> However, other theoretical<sup>106</sup> and experimental<sup>53</sup> work suggest

that structural chirality contributes more significantly to net CD than PCCD in systems that feature anisotropic particles. Wu *et al.* calculated PCCD and structural chirality in simulated molecular-nanoparticle systems and found that structural chirality contributed more significantly to the overall CD signal when the two mechanisms compete in the same systems. <sup>106</sup>

The observed change in CD sign as the globular protein/AuNR ratio was varied suggests the competition of two processes that are governed by protein crowding and conformation.

Supporting this hypothesis are findings that for fibril-templated AuNR assemblies, different Cotton effects were observed when the AuNR aspect ratio was changed. Wang et al. reported based on cryo-TEM that serum albumin-AuNR aggregates were arranged into structurally chiral assemblies with opposite handedness and similarly opposite Cotton effects. Also, Hou et al. showed that AuNR aggregates display opposite Cotton effects due to changes in the twist angle between the AuNRs when L-cysteine selectively adsorbs to AuNR sides versus tips. Rhiols experience a concentration-dependent preference for AuNR sides and tips. Because HSA contains a free thiol, it is possible that preferential protein adsorption to tips versus sides at different concentrations and hence different conformations might play a role in directing the chirality of HSA-AuNR aggregates. On the other hand, studies have shown that the PCCD sign flips due to changes in the chiral molecule's orientation. 400 AuNR sides and tips. 100 AuNR sides are chirality of HSA-AuNR aggregates.

Based on these literature examples that are most similar to our work, we assign structural chirality to be the dominant contributor to our current, ensemble-level observations, but we acknowledge that PCCD cannot be ruled out without further exploration. The observed sign flip likely indicates that different protein conformations under varying conditions of crowding alter the handedness of structurally chiral aggregates. However, it is impossible to separate the possibility that the CD sign flip could result from any combination of changes in the handedness

of structural chirality, variations in PCCD formation, or a switch from PCCD at higher protein/AuNR ratios to structural chirality at lower protein concentrations (based on the CD sign and the behavior of Fib). While our SEM analysis did not distinguish protein-AuNR aggregate geometries among those with opposite CD sign, such distinctions could exist and might be identified with more advanced analysis methods such as cryo-TEM that captures aggregate geometries as present in the solution phase instead of after drying on a substrate. In addition, the different CD contributions mentioned above could likely vary in magnitude when investigating individual aggregates instead.

Fibrous protein-AuNR complexes displayed distinct CD trends from the globular protein-AuNR aggregates that correlate with differences in protein morphology. Because Fib-AuNR complexes did not have positive Cotton effects at protein/AuNR ratios larger than > 5K (while the globular proteins did), we conclude that Fib did not experience crowding effects at the AuNR surface in the same way the globular proteins did. Rather, large fibrous protein superstructures were formed that exceeded the size of the AuNRs, which likely adsorbed to these fibrous protein superstructures. CD from Fib-AuNR aggregates is likely structural chirality, given the morphological similarities to structurally chiral fibril-AuNR assemblies previously reported. We expect PCCD to be less intense in this sample based on the larger spacing between AuNRs, decreasing likelihood of hot-spot enhancements. However, it is worth noting that fibrillar and globular proteins differ in conformation (*i.e.*, fibrillar structures exhibit higher beta-sheet content), and these differences in conformation combined with PCCD could play a role in a protein-AuNR aggregate's net CD.

Although both the fibrillar HSA- and Fib-AuNR aggregates had visible protein superstructures that exceeded the AuNR sizes as determined by SEM, their aggregate shapes and

CD differed. The Fib-AuNR aggregates were long and thin (Figure 5E) and produced net CD (Figure S4D). In contrast, the fibrillar HSA-AuNR sample had a comparatively globular protein aggregate shape (Figure 6C) and did not give CD (Figure S4E). This distinction could be due to the tendency of Fib to aggregate and that its rod-like native structure is better suited to produce long and thin superstructures. HSA had to be forced into fibrils via thermal denaturation. While the resulting protein-AuNR aggregates both contained fibrous protein superstructures, we observed differences in overall aggregate sizes and end-to-end ordering that may contribute to the different chiroptical behavior (Figure S8C). Structurally chiral end-to-end AuNR assemblies made with protein fibrils<sup>99</sup> and glutathione<sup>113</sup> have previously resulted in strong CD. The CD sign and magnitude depend on such parameters as the twist of the protein template as well as the size and aspect ratio of the AuNRs. These results could explain the large CD magnitude we observed for Fib-AuNR aggregates.

#### Micellar CTAB Interferes with Chiral Protein-AuNR Aggregation

To gain further insight into the protein-AuNR aggregation mechanism, we studied how CTAB impacted the chirality of protein-AuNR aggregates. CTAB is a cationic surfactant used in the synthesis and stabilization of AuNRs. Because it is not covalently attached to the AuNRs, its presence could influence protein-AuNR interactions. Further, previous work has suggested that small quantities of CTAB were necessary to achieve a chiroptical signal from BSA-AuNR aggregates.<sup>45</sup>

For all proteins studied, CTAB's presence above the CMC inhibited both AuNR aggregation and CD. Figure 7 shows the extinction and g-factor spectra of IgG-AuNR complexes at IgG/AuNR = 7.1K and 710. When CTAB was below the CMC of 0.92 mM, chiral aggregates

formed. However, when CTAB micelles were present at 5 and 50 mM, the IgG-AuNR mixture did display a CD signal. Additionally, the AuNR extinction did not decrease or redshift when CTAB micelles were present, indicating that the AuNRs did not aggregate. AuNRs were stable at all tested CTAB concentrations (Figure S10). The other protein-AuNR mixtures were also sensitive to CTAB micelle conditions and behaved similarly to the IgG-AuNR samples in Figure 7 in that surfactant concentrations above the CMC prevented aggregation and hence the formation of chiral protein-AuNR complexes. Data for other proteins are provided in Figures S11-13, and additional experiments with CTAB and CTAC are summarized in Figure S14.

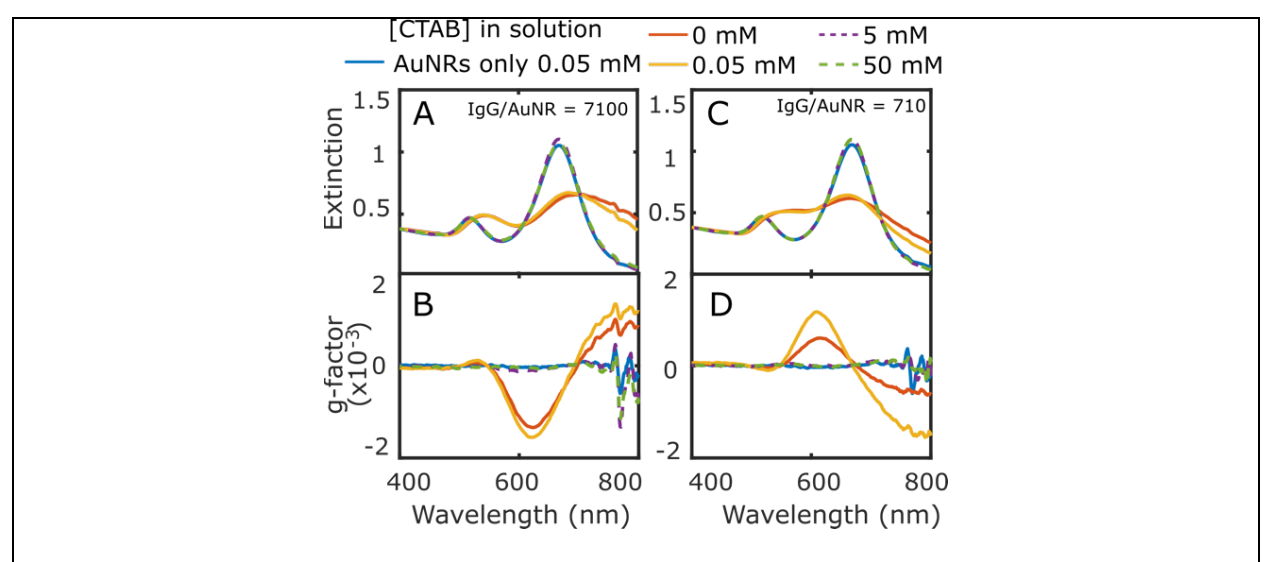


Figure 7: CD spectroscopy of IgG-AuNR complexes with [CTAB] below and above the CMC. Extinction and g-factor spectra for (A-B) IgG/AuNR = 7100 and IgG/AuNR = 710 (C-D). The spectra for AuNRs in 0.05 mM CTAB are included for reference. CD-active IgG-AuNR complexes were only seen in the absence of CTAB micelles. All samples were measured ~30 sec after IgG and AuNRs were combined. Extinction spectra were normalized at 400 nm relative to the AuNR-only sample.

The lack of protein-AuNR aggregation observed in the presence of CTAB micelles supports our hypothesis that both protein-AuNR and protein-protein interactions are necessary to drive aggregation and CD. CTAB likely influences both steps. Because CTAB's presence has been shown to decrease HSA's net negative charge,<sup>44</sup> it is expected that the electrostatic attraction to the cationic AuNRs decreases as the concentration of CTAB increases. All of the other proteins we studied also have net negative charge at physiological conditions,<sup>77</sup> and thus likely have decreased electrostatic attraction for the AuNRs at higher CTAB concentrations.

In addition, intermolecular interactions are crucial for biomolecule-driven AuNR aggregation. He Previous work showed that CTAB's cationic and hydrophobic regions interact with BSA to denature it, such that regions of the protein are stuck within the micelles' hydrophobic cores. He has a protein-protein interactions could also be decreased at higher CTAB concentrations. Furthermore, we were able to rule out that the CTAB micelles themselves prevent AuNR aggregation because the addition of salt caused AuNR aggregation even above the CMC. (Figure S15).

It has been demonstrated that biomolecule-biomolecule interactions are critical for the formation of structurally chiral glutathione (GSH)-AuNR assemblies. <sup>105</sup> Lu *et al.* reported that the tripeptide GSH templated chiral AuNR assembly more efficiently when CTAB micelles were present versus when they were absent. <sup>105</sup> The increased CD from GSH-AuNR aggregates was attributed to improved self-association between GSH molecules instigated by GSH's hydrophobic confinement within micelles. GSH, which has both cationic and anionic components, relies on electrostatic interactions for self-association. In contrast, HSA self-association relies on hydrophobic interactions, and HSA fibrils were disrupted by CTAB micelles, confirming that CTAB above the CMC interferes with HSA-HSA interactions. <sup>115</sup> Thus,

CTAB micelles promoted GSH-induced AuNR aggregation<sup>105</sup> but inhibited HSA-induced AuNR aggregation.

Below the CMC, CTAB differently affected globular and fibrous proteins, providing further evidence that the differently shaped proteins follow different protein-AuNR aggregation mechanisms. At concentrations below the CMC, CTAB can decrease proteins' net negative charge<sup>44</sup> and decrease molar ellipticity (Figure S16). For the globular proteins, there were a few instances where CTAB appeared to increase the CD displayed by protein-AuNR aggregates (Figures 8 & S14). We speculate that this phenomenon could be related to CTAB denaturing the globular proteins in a way that facilitated protein-AuNR aggregation. Fib, in contrast, had larger g-factors in the absence of CTAB, which could indicate that CTAB interferes with the formation of Fib superstructures that template AuNR assembly.

#### Conclusion

In this study, we reported the effects of protein identity, protein/AuNR ratio, and CTAB solution chemistry on the CD of protein-AuNR aggregates. First, we found that HSA was not unique in its ability to produce chiral AuNR complexes, because IgG, Tf, and Fib also templated AuNR aggregation. Second, experimental evidence suggests that the globular proteins (HSA, IgG, and Tf) follow a similar aggregation mechanism. Globular protein-AuNR aggregates had positive Cotton effects above a unique critical protein/AuNR ratio and negative Cotton effects below. We propose that changes in protein conformation due to increased or decreased crowding on the AuNR surface preferentially produce AuNR assemblies of opposite-handedness. We suspect structural chirality to be the more likely mechanism of CD formation but cannot rule out contributions from PCCD.

Third, we found that the fibrous protein-AuNR aggregation mechanism deviated from that of the globular proteins. Fib-AuNR assemblies did not exhibit a CD sign flip as the Fib/AuNR ratio varied, distinguishing Fib, a fibrous protein, from the globular proteins. Further, SEM revealed fibrous Fib superstructures that exceeded the dimensions of the AuNRs, and we pose that these structures created a template for AuNR adsorption. Further, fibrillar HSA-AuNR aggregates were more similar to Fib-AuNR aggregates based on their overall chiroptical properties as a function of protein/AuNR ratio in addition to the size of the HSA fibrils also exceeding the dimensions of the AuNRs.

Fourth, we revealed that protein-AuNR aggregation is sensitive to the CTAB concentration and to the presence or absence of surfactant micelles. At concentrations above the CMC, CTAB inhibited protein-induced AuNR aggregation altogether, which could be linked to both interruption of protein-AuNR electrostatic attraction as well as hydrophobic protein-protein association. Below the CMC, we found evidence that CTAB enhances CD in some globular protein-AuNR aggregates but inhibits CD in fibrous protein-AuNR aggregates.

The results presented here do not permit a definitive mechanism for protein-AuNR chiral aggregation. However, we have surveyed a large parameter space including protein shape, charge, size, protein/AuNR ratios, and the ability of a micellar surfactant to prevent protein-protein interactions. Our results support a mechanism in which adsorption-induced protein conformational changes followed by protein-protein interactions are an important driving factor in observed CD sign and amplitude. Future studies that combine cryo-TEM microscopy and tomography<sup>44-45, 105</sup> with single-particle scattering spectroscopy and simulations<sup>45</sup> are needed to move towards the goal of a full and quantitative description.

# **Supporting Information Description**

The Supporting Information is available free of charge at

Particle size analysis of AuNRs; reproducibility of protein/gold nanorod ratio experiments; two-sample K-S comparison for non-normal data; sample statistics from scanning electron microscopy aggregate analysis; side-by-side ordering of globular protein-AuNR aggregates from SEM micrographs; extinction and circular dichroism spectra corresponding to the samples studied by SEM; native proteins' far UV CD; HSA-AuNR aggregate CD spectra with and without the salt present in Fib samples; Fib superstructures even in the absence of AuNRs; size and geometric ordering of fibrous protein-AuNR aggregates from SEM micrographs; HSA fibrillation characterization; AuNR solutions with varying CTAB concentrations; sample trial for HSA-AuNR study with varying CTAB concentrations; sample trial for Tf-AuNR study with varying CTAB concentrations; averaged maximum g-factors observed for AuNR aggregates with positive and negative Cotton effects as a function of CTAB or CTAC concentration; AuNR aggregation from salt when CTAB was present above or below the CMC; protein secondary structure as a function of surfactant concentration; other experimental details

# Acknowledgment

This work was supported by the Robert A. Welch Foundation (C-1787 to C. F. L.) and the National Science Foundation (CHE-1903980 to S. L.). S.L thanks the Robert A. Welch Foundation for support through the Charles W. Duncan, Jr.-Welch Chair in Chemistry (C-0002). The authors thank Dr. Qingfeng Zhang and Dr. Rashad Baiyasi for stimulating discussions. This work was conducted in part using resources of the Shared Equipment Authority at Rice University.

#### References

- 1. Paule Pileni, M. Optical Properties of Nanosized Particles Dispersed in Colloidal Solutions or Arranged in 2d or 3d Superlattices. *New J. Chem.* **1998,** *22*, 693-702.
- 2. Pileni, M.-P. The Role of Soft Colloidal Templates in Controlling the Size and Shape of Inorganic Nanocrystals. *Nat. Mater.* **2003**, *2*, 145-150.
- 3. Sun, Y.;Xia, Y. Shape-Controlled Synthesis of Gold and Silver Nanoparticles. *Science* **2002**, *298*, 2176-2179.
- 4. Qin, D.; Xia, Y.; Whitesides, G. M. Soft Lithography for Micro-and Nanoscale Patterning. *Nat. Protoc.* **2010**, *5*, 491.
- 5. Karst, J.; Strohfeldt, N.; Schaferling, M.; Giessen, H.; Hentschel, M. Single Plasmonic Oligomer Chiral Spectroscopy. *Adv. Opt. Mater.* **2018**, *6*.
- 6. Bochenkov, V. E.; Shabatina, T. I. Chiral Plasmonic Biosensors. *Biosensors-Basel* **2018**, 8.
- 7. Cai, J.; Hao, C.; Sun, M.; Ma, W.; Xu, C.; Kuang, H. Chiral Shell Core—Satellite Nanostructures for Ultrasensitive Detection of Mycotoxin. *Small* **2018**, *14*, 1703931.
- 8. Yan, W. J.; Wang, Y. L.; Zhuang, H.; Zhang, J. H. DNA-Engineered Chiroplasmonic Heteropyramids for Ultrasensitive Detection of Mercury Ion. *Biosens. Bioelectron.* **2015**, *68*, 516-520.
- 9. Frank, B.; Yin, X.; Schäferling, M.; Zhao, J.; Hein, S. M.; Braun, P. V.; Giessen, H. Large-Area 3d Chiral Plasmonic Structures. *ACS Nano* **2013**, *7*, 6321-6329.
- 10. Xu, Z.; Xu, L.; Zhu, Y.; Ma, W.; Kuang, H.; Wang, L.; Xu, C. Chirality Based Sensor for Bisphenol a Detection. *Chem. Commun.* **2012**, *48*, 5760-5762.
- 11. Tang, L.; Li, S.; Xu, L.; Ma, W.; Kuang, H.; Wang, L.; Xu, C. Chirality-Based Au@Ag Nanorod Dimers Sensor for Ultrasensitive Psa Detection. *ACS Appl. Mater. Interfaces* **2015**, *7*, 12708-12712.
- 12. Funck, T.; Nicoli, F.; Kuzyk, A.; Liedl, T. Sensing Picomolar Concentrations of Rna Using Switchable Plasmonic Chirality. *Angew. Chem. Int. Ed.* **2018**, *57*, 13495-13498.
- 13. Liu, T. J.; Besteiro, L. V.; Liedl, T.; Correa-Duarte, M. A.; Wang, Z. M.; Govorov, A. O. Chiral Plasmonic Nanocrystals for Generation of Hot Electrons: Toward Polarization-Sensitive Photochemistry. *Nano Lett.* **2019**, *19*, 1395-1407.
- 14. Khorashad, L. K.; Besteiro, L. V.; Correa-Duarte, M. A.; Burger, S.; Wang, Z. M.; Govorov, A. O. Hot Electrons Generated in Chiral Plasmonic Nanocrystals as a Mechanism for Surface Photochemistry and Chiral Growth. *J. Am. Chem. Soc.* **2020**, *142*, 4193-4205.
- 15. Esteban, P.-V.; Francesco, P.; Alexandre, D. Perspective: Plasmon Antennas for Nanoscale Chiral Chemistry. *Nanophotonics* **2020**, *9*, 481-489.
- 16. Hao, C.; Xu, L.; Ma, W.; Wu, X.; Wang, L.; Kuang, H.; Xu, C. Unusual Circularly Polarized Photocatalytic Activity in Nanogapped Gold–Silver Chiroplasmonic Nanostructures. *Adv. Funct. Mater.* **2015**, *25*, 5816-5822.
- 17. Grzelczak, M.; Vermant, J.; Furst, E. M.;Liz-Marzán, L. M. Directed Self-Assembly of Nanoparticles. *ACS Nano* **2010**, *4*, 3591-3605.
- 18. Soukoulis, C. M.; Wegener, M. Past Achievements and Future Challenges in the Development of Three-Dimensional Photonic Metamaterials. *Nat. Photonics* **2011**, *5*, 523-530.
- 19. Zhang, Q.; Gu, J.; Zhang, L.;Lin, J. Diverse Chiral Assemblies of Nanoparticles Directed by Achiral Block Copolymers Via Nanochannel Confinement. *Nanoscale* **2019**, *11*, 474-484.

- 20. Zhou, Y.; Marson, R. L.; van Anders, G.; Zhu, J.; Ma, G.; Ercius, P.; Sun, K.; Yeom, B.; Glotzer, S. C.; Kotov, N. A. Biomimetic Hierarchical Assembly of Helical Supraparticles from Chiral Nanoparticles. *ACS Nano* **2016**, *10*, 3248-3256.
- 21. Mao, X.; Zhan, Y.; Wang, Y.; Li, Q.; Wang, Z.; Zeng, D.; Cao, H.; Shen, Y.; Wang, J. Self-Assembled Chiral Nanoparticles Superstructures and Identification of Their Collective Optical Activity from Ligand Asymmetry. *ACS Nano* **2020**, *14*, 1208-1208.
- 22. Chu, G.; Wang, X.; Chen, T.; Gao, J.; Gai, F.; Wang, Y.; Xu, Y. Optically Tunable Chiral Plasmonic Guest–Host Cellulose Films Weaved with Long-Range Ordered Silver Nanowires. *ACS Appl. Mater. Interfaces* **2015**, *7*, 11863-11870.
- 23. Querejeta-Fernández, A.; Kopera, B.; Prado, K. S.; Klinkova, A.; Methot, M.; Chauve, G.; Bouchard, J.; Helmy, A. S.; Kumacheva, E. Circular Dichroism of Chiral Nematic Films of Cellulose Nanocrystals Loaded with Plasmonic Nanoparticles. *ACS Nano* **2015**, *9*, 10377-10385.
- 24. Liu, Q.; Campbell, M. G.; Evans, J. S.; Smalyukh, I. I. Orientationally Ordered Colloidal Co-Dispersions of Gold Nanorods and Cellulose Nanocrystals. *Adv. Mater.* **2014**, *26*, 7178-7184.
- 25. Querejeta-Fernández, A.; Chauve, G.; Methot, M.; Bouchard, J.; Kumacheva, E. Chiral Plasmonic Films Formed by Gold Nanorods and Cellulose Nanocrystals. *J. Am. Chem. Soc.* **2014**, *136*, 4788-4793.
- 26. Kaushik, M.; Basu, K.; Benoit, C.; Cirtiu, C. M.; Vali, H.; Moores, A. Cellulose Nanocrystals as Chiral Inducers: Enantioselective Catalysis and Transmission Electron Microscopy 3d Characterization. *J. Am. Chem. Soc.* **2015**, *137*, 6124-6127.
- 27. Guerrero-Martínez, A.; Auguié, B.; Alonso-Gómez, J. L.; Džolić, Z.; Gómez-Graña, S.; Žinić, M.; Cid, M. M.;Liz-Marzán, L. M. Intense Optical Activity from Three-Dimensional Chiral Ordering of Plasmonic Nanoantennas. *Angew. Chem. Int. Ed. Engl.* **2011**, *50*, 5499-5503.
- 28. Oh, H. S.; Liu, S.; Jee, H.; Baev, A.; Swihart, M. T.; Prasad, P. N. Chiral Poly(Fluorene-Alt-Benzothiadiazole) (Pfbt) and Nanocomposites with Gold Nanoparticles: Plasmonically and Structurally Enhanced Chirality. *J. Am. Chem. Soc.* **2010**, *132*, 17346-17348.
- 29. Baimuratov, A. S.; Rukhlenko, I. D.; Noskov, R. E.; Ginzburg, P.; Gun'ko, Y. K.; Baranov, A. V.; Fedorov, A. V. Giant Optical Activity of Quantum Dots, Rods, and Disks with Screw Dislocations. *Sci. Rep.* **2015**, *5*.
- 30. Jung, S. H.; Jeon, J.; Kim, H.; Jaworski, J.; Jung, J. H. Chiral Arrangement of Achiral Au Nanoparticles by Supramolecular Assembly of Helical Nanofiber Templates. *J. Am. Chem. Soc.* **2014**, *136*, 6446-6452.
- 31. Han, B.; Shi, L.; Gao, X.; Guo, J.; Hou, K.; Zheng, Y.; Tang, Z. Ultra-Stable Silica-Coated Chiral Au-Nanorod Assemblies: Core—Shell Nanostructures with Enhanced Chiroptical Properties. *Nano Research* **2016**, *9*, 451-457.
- 32. Hou, S.; Wen, T.; Zhang, H.; Liu, W.; Hu, X.; Wang, R.; Hu, Z.; Wu, X. Fabrication of Chiral Plasmonic Oligomers Using Cysteine-Modified Gold Nanorods as Monomers. *Nano Research* **2014**, *7*, 1699-1705.
- 33. Chen, L.; Zheng, J.; Feng, J.; Qian, Q.; Zhou, Y. Reversible Modulation of Plasmonic Chiral Signals of Achiral Gold Nanorods Using a Chiral Supramolecular Template. *Chem. Commun* **2019**, *55*, 11378-11381.
- 34. Merg, A. D.; Boatz, J. C.; Mandal, A.; Zhao, G. P.; Mokashi-Punekar, S.; Liu, C.; Wang, X. T.; Zhang, P. J.; van der Wel, P. C. A.;Rosi, N. L. Peptide-Directed Assembly of Single-Helical Gold Nanoparticle Superstructures Exhibiting Intense Chiroptical Activity. *J. Am. Chem. Soc.* **2016**, *138*, 13655-13663.

- 35. Song, C.; Blaber, M. G.; Zhao, G.; Zhang, P.; Fry, H. C.; Schatz, G. C.;Rosi, N. L. Tailorable Plasmonic Circular Dichroism Properties of Helical Nanoparticle Superstructures. *Nano Lett.* **2013**, *13*, 3256-3261.
- 36. Chen, C.-L.; Zhang, P.;Rosi, N. L. A New Peptide-Based Method for the Design and Synthesis of Nanoparticle Superstructures: Construction of Highly Ordered Gold Nanoparticle Double Helices. *J. Am. Chem. Soc.* **2008**, *130*, 13555-13557.
- 37. Ma, W.; Kuang, H.; Wang, L.; Xu, L.; Chang, W.-S.; Zhang, H.; Sun, M.; Zhu, Y.; Zhao, Y.; Liu, L., et al. Chiral Plasmonics of Self-Assembled Nanorod Dimers. *Sci. Rep.* **2013**, *3*, 1934.
- 38. Zhu, Z.; Liu, W.; Li, Z.; Han, B.; Zhou, Y.; Gao, Y.; Tang, Z. Manipulation of Collective Optical Activity in One-Dimensional Plasmonic Assembly. *ACS Nano* **2012**, *6*, 2326-2332.
- 39. Chen, C.-L.;Rosi, N. L. Preparation of Unique 1-D Nanoparticle Superstructures and Tailoring Their Structural Features. *J. Am. Chem. Soc.* **2010**, *132*, 6902-6903.
- 40. Hentschel, M.; Schaferling, M.; Metzger, B.; Giessen, H. Plasmonic Diastereomers: Adding up Chiral Centers. *Nano Lett.* **2013**, *13*, 600-606.
- 41. Liu, J. J.; Yang, L.; Huang, Z. F. Chiroptically Active Plasmonic Nanoparticles Having Hidden Helicity and Reversible Aqueous Solvent Effect on Chiroptical Activity. *Small* **2016**, *12*, 5902-5909.
- 42. Merg, A. D.; Slocik, J.; Blaber, M. G.; Schatz, G. C.; Naik, R.;Rosi, N. L. Adjusting the Metrics of 1-D Helical Gold Nanoparticle Superstructures Using Multivalent Peptide Conjugates. *Langmuir* **2015**, *31*, 9492-9501.
- 43. Mokashi-Punekar, S.;Rosi, N. L. Deliberate Introduction of Particle Anisotropy in Helical Gold Nanoparticle Superstructures. *Part. Syst. Charact.* **2019**, *36*.
- 44. Shinmori, H.; Mochizuki, C. Strong Chiroptical Activity from Achiral Gold Nanorods Assembled with Proteins. *Chem. Commun.* **2017**, *53*, 6569-6572.
- 45. Zhang, Q.; Hernandez, T.; Smith, K. W.; Jebeli, S. A. H.; Dai, A. X.; Warning, L.; Baiyasi, R.; McCarthy, L. A.; Guo, H.; Chen, D.-H., et al. Unraveling the Origin of Chirality from Plasmonic Nanoparticle-Protein Complexes. *Science* **2019**.
- 46. Dominguez-Medina, S.; Kisley, L.; Tauzin, L. J.; Hoggard, A.; Shuang, B.; Indrasekara, A. S.; Chen, S.; Wang, L. Y.; Derry, P. J.; Liopo, A., et al. Adsorption and Unfolding of a Single Protein Triggers Nanoparticle Aggregation. *ACS Nano* **2016**, *10*, 2103-2112.
- 47. Satzer, P.; Svec, F.; Sekot, G.; Jungbauer, A. Protein Adsorption onto Nanoparticles Induces Conformational Changes: Particle Size Dependency, Kinetics, and Mechanisms. *Eng. Life Sci.* **2016**, *16*, 238-246.
- 48. Walkey, C. D.; Olsen, J. B.; Guo, H.; Emili, A.; Chan, W. C. W. Nanoparticle Size and Surface Chemistry Determine Serum Protein Adsorption and Macrophage Uptake. *J. Am. Chem. Soc.* **2012**, *134*, 2139-2147.
- 49. Gessner, A.; Waicz, R.; Lieske, A.; Paulke, B. R.; Mäder, K.; Müller, R. H. Nanoparticles with Decreasing Surface Hydrophobicities: Influence on Plasma Protein Adsorption. *Int. J. Pharm.* **2000**, *196*, 245-249.
- 50. Bell, N. C.; Minelli, C.; Shard, A. G. Quantitation of Igg Protein Adsorption to Gold Nanoparticles Using Particle Size Measurement. *Anal. Methods* **2013**, *5*, 4591-4601.
- 51. Pan, H.; Qin, M.; Meng, W.; Cao, Y.; Wang, W. How Do Proteins Unfold Upon Adsorption on Nanoparticle Surfaces? *Langmuir* **2012**, *28*, 12779-12787.
- 52. Deng, Z. J.; Liang, M.; Monteiro, M.; Toth, I.; Minchin, R. F. Nanoparticle-Induced Unfolding of Fibrinogen Promotes Mac-1 Receptor Activation and Inflammation. *Nat. Nanotechnol.* **2011**, *6*, 39-44.

- 53. Wang, Z.-Y.; Zhang, N.-N.; Li, J.-C.; Lu, J.; Zhao, L.; Fang, X.-D.; Liu, K. Serum Albumin Guided Plasmonic Nanoassemblies with Opposite Chiralities. *Soft Matter* **2021**, *17*, 6298-6304.
- 54. Govorov, A. O. Plasmon-Induced Circular Dichroism of a Chiral Molecule in the Vicinity of Metal Nanocrystals. Application to Various Geometries. *J. Phys. Chem. C* **2011**, *115*, 7914-7923.
- 55. Levi-Belenkova, T.; Govorov, A. O.; Markovich, G. Orientation-Sensitive Peptide-Induced Plasmonic Circular Dichroism in Silver Nanocubes. *J. Phys. Chem. C* **2016**, *120*, 12751-12756.
- 56. Govorov, A. O.; Fan, Z.; Hernandez, P.; Slocik, J. M.; Naik, R. R. Theory of Circular Dichroism of Nanomaterials Comprising Chiral Molecules and Nanocrystals: Plasmon Enhancement, Dipole Interactions, and Dielectric Effects. *Nano Lett.* **2010**, *10*, 1374-1382.
- 57. Layani, M. E.; Ben Moshe, A.; Varenik, M.; Regev, O.; Zhang, H.; Govorov, A. O.; Markovich, G. Chiroptical Activity in Silver Cholate Nanostructures Induced by the Formation of Nanoparticle Assemblies. *J. Phys. Chem. C* **2013**, *117*, 22240-22244.
- 58. Cukalevski, R.; Ferreira, S. A.; Dunning, C. J.; Berggård, T.; Cedervall, T. Igg and Fibrinogen Driven Nanoparticle Aggregation. *Nano Research* **2015**, *8*, 2733-2743.
- 59. Albanese, A.; Chan, W. C. W. Effect of Gold Nanoparticle Aggregation on Cell Uptake and Toxicity. *ACS Nano* **2011**, *5*, 5478-5489.
- 60. Jamison, J. A.; Bryant, E. L.; Kadali, S. B.; Wong, M. S.; Colvin, V. L.; Matthews, K. S.; Calabretta, M. K. Altering Protein Surface Charge with Chemical Modification Modulates Protein–Gold Nanoparticle Aggregation. *J. Nanopart. Res.* **2011**, *13*, 625-636.
- 61. Walkey, C. D.; Olsen, J. B.; Song, F.; Liu, R.; Guo, H.; Olsen, D. W. H.; Cohen, Y.; Emili, A.; Chan, W. C. W. Protein Corona Fingerprinting Predicts the Cellular Interaction of Gold and Silver Nanoparticles. *ACS Nano* **2014**, *8*, 2439-2455.
- 62. Lynch, I.; Dawson, K. A. Protein-Nanoparticle Interactions. *Nano Today* **2008**, *3*, 40-47.
- 63. Vigderman, L.; Manna, P.; Zubarev, E. R. Quantitative Replacement of Cetyl Trimethylammonium Bromide by Cationic Thiol Ligands on the Surface of Gold Nanorods and Their Extremely Large Uptake by Cancer Cells. *Angew. Chem. Int. Ed.* **2012**, *51*, 636-641.
- 64. Smith, D. K.; Korgel, B. A. The Importance of the Ctab Surfactant on the Colloidal Seed-Mediated Synthesis of Gold Nanorods. *Langmuir* **2008**, *24*, 644-649.
- 65. Mukerjee, P.;Mysels, K. J. *Critical Micelle Concentrations of Aqueous Surfactant Systems*; National Standard reference data system: 1971.
- 66. Bhattacharya, M.; Jain, N.; Mukhopadhyay, S. Insights into the Mechanism of Aggregation and Fibril Formation from Bovine Serum Albumin. *J. Phys. Chem. B* **2011**, *115*, 4195-4205.
- 67. Juárez, J.; Taboada, P.; Mosquera, V. Existence of Different Structural Intermediates on the Fibrillation Pathway of Human Serum Albumin. *Biophys. J.* **2009**, *96*, 2353-2370.
- 68. Kuhn, W. Optical Rotatory Power. Annu. Rev. Phys. Chem. 1958, 9, 417-438.
- 69. Baiyasi, R.; Gallagher, M. J.; McCarthy, L. A.; Searles, E. K.; Zhang, Q.; Link, S.; Landes, C. F. Quantitative Analysis of Nanorod Aggregation and Morphology from Scanning Electron Micrographs Using Semseg. *J. Phys. Chem. A* **2020**, *124*, 5262-5270.
- 70. Wians, F. Blood Tests: Normal Values. https://www.merckmanuals.com/professional/resources/normal-laboratory-values/blood-tests-normal-values (accassed 2021).

- 71. Prescott, S. W.; Mulvaney, P. Gold Nanorod Extinction Spectra. J. Appl. Phys. **2006**, 99, 123504.
- 72. Pérez-Juste, J.; Pastoriza-Santos, I.; Liz-Marzán, L. M.; Mulvaney, P. Gold Nanorods: Synthesis, Characterization and Applications. *Coord. Chem. Rev.* **2005**, *249*, 1870-1901.
- 73. Carreira, E. M.; Yamamoto, H.; *Comprehensive Chirality*; Elsevier: Amsterdam, 2012.
- 74. Sugio, S.; Kashima, A.; Mochizuki, S.; Noda, M.; Kobayashi, K. Crystal Structure of Human Serum Albumin at 2.5 Å Resolution. *Protein Eng. Des. Sel.* **1999**, *12*, 439-446.
- 75. Harris, L. J.; Larson, S. B.; Hasel, K. W.; McPherson, A. Refined Structure of an Intact Igg2a Monoclonal Antibody. *Biochemistry* **1997**, *36*, 1581-1597.
- 76. Wally, J.; Halbrooks, P. J.; Vonrhein, C.; Rould, M. A.; Everse, S. J.; Mason, A. B.; Buchanan, S. K. The Crystal Structure of Iron-Free Human Serum Transferrin Provides Insight into Inter-Lobe Communication and Receptor Binding. *J. Biol. Chem.* **2006**, *281*, 24934-24944.
- 77. Anderson, N. L.; Anderson, N. G. The Human Plasma Proteome. *Mol. Cell. Proteomics* **2002,** *1*, 845.
- 78. He, X. M.; Carter, D. C. Atomic Structure and Chemistry of Human Serum Albumin. *Nature* **1993**, *364*, 362-362.
- 79. Bailey, S.; Evans, R. W.; Garratt, R. C.; Gorinsky, B.; Hasnain, S.; Horsburgh, C.; Jhoti, H.; Lindley, P. F.;Mydin, A. Molecular Structure of Serum Transferrin at 3.3-.Ang. Resolution. *Biochemistry* **1988**, *27*, 5804-5812.
- 80. Armstrong, J. K.; Wenby, R. B.; Meiselman, H. J.; Fisher, T. C. The Hydrodynamic Radii of Macromolecules and Their Effect on Red Blood Cell Aggregation. *Biophys. J.* **2004**, *87*, 4259-4270.
- 81. Tan, Y. H.; Liu, M.; Nolting, B.; Go, J. G.; Gervay-Hague, J.; Liu, G.-y. A Nanoengineering Approach for Investigation and Regulation of Protein Immobilization. *ACS Nano* **2008**, *2*, 2374-2384.
- 82. Jøssang, T.; Feder, J.;Rosenqvist, E. Photon Correlation Spectroscopy of Human Igg. *J. Protein Chem.* **1988,** *7*, 165-171.
- 83. Hall, C. E.; Slayter, H. S. The Fibrinogen Molecule: Its Size, Shape, and Mode of Polymerization. *J. Biophys. Biochem. Cytol.* **1959**, *5*, 11-16.
- 84. Kollman, J. M.; Pandi, L.; Sawaya, M. R.; Riley, M.; Doolittle, R. F. Crystal Structure of Human Fibrinogen. *Biochemistry* **2009**, *48*, 3877-3886.
- 85. Kneer, L. M.; Roller, E.-M.; Besteiro, L. V.; Schreiber, R.; Govorov, A. O.; Liedl, T. Circular Dichroism of Chiral Molecules in DNA-Assembled Plasmonic Hotspots. *ACS Nano* **2018**, *12*, 9110-9115.
- 86. Kuzyk, A.; Schreiber, R.; Zhang, H.; Govorov, A. O.; Liedl, T.;Liu, N. Reconfigurable 3d Plasmonic Metamolecules. *Nat Mater.* **2014**, *13*, 862-866.
- 87. Matsui, N.; Nozaki, K.; Ishihara, K.; Yamashita, K.; Nagai, A. Concentration-Dependent Effects of Fibronectin Adsorbed on Hydroxyapatite Surfaces on Osteoblast Adhesion. *Mater. Sci. Eng. C Mater. Biol. Appl.* **2015**, *48*, 378-383.
- 88. Zhou, H.-X.; Rivas, G.;Minton, A. P. Macromolecular Crowding and Confinement: Biochemical, Biophysical, and Potential Physiological Consequences. *Annu. Rev. Biophys.* **2008**, *37*, 375-397.
- 89. Guin, D.; Gruebele, M. Weak Chemical Interactions That Drive Protein Evolution: Crowding, Sticking, and Quinary Structure in Folding and Function. *Chem. Rev.* **2019**, *119*, 10691-10717.

- 90. Michael, K. E.; Vernekar, V. N.; Keselowsky, B. G.; Meredith, J. C.; Latour, R. A.; García, A. J. Adsorption-Induced Conformational Changes in Fibronectin Due to Interactions with Well-Defined Surface Chemistries. *Langmuir* **2003**, *19*, 8033-8040.
- 91. Keselowsky, B. G.; Collard, D. M.; García, A. J. Surface Chemistry Modulates Fibronectin Conformation and Directs Integrin Binding and Specificity to Control Cell Adhesion. *J. Biomed. Mater. Res. A* **2003**, *66*, 247-259.
- 92. Sun, B.; Zhang, Y.; Chen, W.; Wang, K.; Zhu, L. Concentration Dependent Effects of Bovine Serum Albumin on Graphene Oxide Colloidal Stability in Aquatic Environment. *Environ. Sci. Technol.* **2018**, *52*, 7212-7219.
- 93. Wang, H.; Ma, R.; Nienhaus, K.; Nienhaus, G. U. Formation of a Monolayer Protein Corona around Polystyrene Nanoparticles and Implications for Nanoparticle Agglomeration. **2019**, *15*, e1900974.
- 94. Levak, M.; Burić, P.; Dutour Sikirić, M.; Domazet Jurašin, D.; Mikac, N.; Bačić, N.; Drexel, R.; Meier, F.; Jakšić, Ž.;Lyons, D. M. Effect of Protein Corona on Silver Nanoparticle Stabilization and Ion Release Kinetics in Artificial Seawater. *Environ. Sci. Technol.* **2017**, *51*, 1259-1266.
- 95. Dominguez-Medina, S.; Blankenburg, J.; Olson, J.; Landes, C. F.; Link, S. Adsorption of a Protein Monolayer Via Hydrophobic Interactions Prevents Nanoparticle Aggregation under Harsh Environmental Conditions. *ACS Sustainable Chem. Eng.* **2013**, *1*, 833-842.
- 96. Shang, L.; Nienhaus, G. U. In Situ Characterization of Protein Adsorption onto Nanoparticles by Fluorescence Correlation Spectroscopy. *Acc. Chem. Res.* **2017**, *50*, 387-395.
- 97. Gui, L.; Hentschel, M.; Defrance, J.; Krauth, J.; Weiss, T.; Giessen, H. Nonlinear Born-Kuhn Analog for Chiral Plasmonics. *ACS Photonics* **2019**, *6*, 3306-3314.
- 98. Chen, Z.; Lan, X.; Chiu, Y.-C.; Lu, X.; Ni, W.; Gao, H.; Wang, Q. Strong Chiroptical Activities in Gold Nanorod Dimers Assembled Using DNA Origami Templates. *ACS Photonics* **2015**, *2*, 392-397.
- 99. Lu, J.; Xue, Y.; Bernardino, K.; Zhang, N.-N.; Gomes, W. R.; Ramesar, N. S.; Liu, S.; Hu, Z.; Sun, T.; de Moura, A. F., et al. Enhanced Optical Asymmetry in Supramolecular Chiroplasmonic Assemblies with Long-Range Order. *Science* **2021**, *371*, 1368.
- 100. Martens, K.; Binkowski, F.; Nguyen, L.; Hu, L.; Govorov, A. O.; Burger, S.; Liedl, T. Long- and Short-Ranged Chiral Interactions in DNA-Assembled Plasmonic Chains. *Nat. Commun.* **2021**, *12*, 2025.
- 101. Lan, X.; Chen, Z.; Dai, G.; Lu, X.; Ni, W.; Wang, Q. Bifacial DNA Origami-Directed Discrete, Three-Dimensional, Anisotropic Plasmonic Nanoarchitectures with Tailored Optical Chirality. *J. Am. Chem. Soc.* **2013**, *135*, 11441-11444.
- 102. Maoz, B. M.; Chaikin, Y.; Tesler, A. B.; Bar Elli, O.; Fan, Z.; Govorov, A. O.; Markovich, G. Amplification of Chiroptical Activity of Chiral Biomolecules by Surface Plasmons. *Nano Lett.* **2013**, *13*, 1203-1209.
- 103. Zhu, F.; Li, X.; Li, Y.; Yan, M.; Liu, S. Enantioselective Circular Dichroism Sensing of Cysteine and Glutathione with Gold Nanorods. *Anal. Chem.* **2015**, *87*, 357-361.
- 104. Severoni, E.; Maniappan, S.; Liz-Marzán, L. M.; Kumar, J.; García de Abajo, F. J.; Galantini, L. Plasmon-Enhanced Optical Chirality through Hotspot Formation in Surfactant-Directed Self-Assembly of Gold Nanorods. *ACS Nano* **2020**, *14*, 16712-16722.
- 105. Lu, J.; Chang, Y.-X.; Zhang, N.-N.; Wei, Y.; Li, A.-J.; Tai, J.; Xue, Y.; Wang, Z.-Y.; Yang, Y.; Zhao, L., et al. Chiral Plasmonic Nanochains Via the Self-Assembly of Gold Nanorods

- and Helical Glutathione Oligomers Facilitated by Cetyltrimethylammonium Bromide Micelles. *ACS Nano* **2017**, *11*, 3463-3475.
- 106. Wu, T.; Ren, J.; Wang, R.; Zhang, X. Competition of Chiroptical Effect Caused by Nanostructure and Chiral Molecules. *J. Phys. Chem. C* **2014**, *118*, 20529-20537.
- 107. Kumar, J.; Eraña, H.; López-Martínez, E.; Claes, N.; Martín, V. F.; Solís, D. M.; Bals, S.; Cortajarena, A. L.; Castilla, J.; Liz-Marzán, L. M. Detection of Amyloid Fibrils in Parkinson's Disease Using Plasmonic Chirality. *Proc. Natl. Acad. Sci. U.S.A.* **2018**, *115*, 3225.
- 108. Hou, S.; Zhang, H.; Yan, J.; Ji, Y.; Wen, T.; Liu, W.; Hu, Z.; Wu, X. Plasmonic Circular Dichroism in Side-by-Side Oligomers of Gold Nanorods: The Influence of Chiral Molecule Location and Interparticle Distance. *PCCP* **2015**, *17*, 8187-8193.
- 109. Kou, X.; Zhang, S.; Yang, Z.; Tsung, C.-K.; Stucky, G. D.; Sun, L.; Wang, J.; Yan, C. Glutathione- and Cysteine-Induced Transverse Overgrowth on Gold Nanorods. *J. Am. Chem. Soc.* **2007**, *129*, 6402-6404.
- 110. Nakashima, H.; Furukawa, K.; Kashimura, Y.; Torimitsu, K. Anisotropic Assembly of Gold Nanorods Assisted by Selective Ion Recognition of Surface-Anchored Crown Ether Derivatives. *Chem. Commun* **2007**, 1080-1082.
- 111. Longo, E.; Orlandin, A.; Mancin, F.; Scrimin, P.; Moretto, A. Reversible Chirality Control in Peptide-Functionalized Gold Nanoparticles. *ACS Nano* **2013**, *7*, 9933-9939.
- 112. Kumar, J.; Erana, H.; Lopez-Martinez, E.; Claes, N.; Martin, V. F.; Solis, D. M.; Bals, S.; Cortajarena, A. L.; Castilla, J.;Liz-Marzán, L. M. Detection of Amyloid Fibrils in Parkinson's Disease Using Plasmonic Chirality. *Proc. Natl. Acad. Sci. U. S. A.* **2018**, *115*, 3225-3230.
- 113. Lu, J.; Chang, Y. X.; Zhang, N. N.; Wei, Y.; Li, A. J.; Tai, J.; Xue, Y.; Wang, Z. Y.; Yang, Y.; Zhao, L., et al. Chiral Plasmonic Nanochains Via the Self-Assembly of Gold Nanorods and Helical Glutathione Oligomers Facilitated by Cetyltrimethylammonium Bromide Micelles. *ACS Nano* **2017**, *11*, 3463-3475.
- 114. Chakraborty, T.; Chakraborty, I.; Moulik, S. P.; Ghosh, S. Physicochemical and Conformational Studies on Bsa–Surfactant Interaction in Aqueous Medium. *Langmuir* **2009**, *25*, 3062-3074.
- 115. Pandey, N. K.; Ghosh, S.;Dasgupta, S. Effect of Surfactants on Preformed Fibrils of Human Serum Albumin. *Int. J. Biol. Macromol.* **2013**, *59*, 39-45.